

Copper, Potassium Promoted Iron on Metallosilicate and Aluminum Oxide Supports Synthesized Via a Non-Hydrolytic Sol-Gel for Fischer-Tropsch

Tugce N. Eran^{*a}, Federico Galli^b, Jean Guyot^a, Josianne Lefebvre^a, Arian Grainca^c, Gregory Patience^a, Carlo Pirola^c

^a*Polytechnique Montréal, Chemical Engineering, CP 6079, Succ CV, Montréal, Québec H3C 3A7, Canada*

^b*Université de Sherbrooke, Génie Chimique et de Génie Biotechnologique, 2500 Boul. de l'Université, Sherbrooke, Québec J1K 2R1, Canada*

^c*Università degli Studi di Milano, Chimica, via Golgi 19, 20133 Milano, Italy*

Abstract

We developed a promoted iron based catalyst that converts 20% more CO to diesel than the unpromoted counterparts. The synthesis involves a non-hydrolytic sol-gel method (NHSG) and 0.04 g g⁻¹ copper and 0.02 g g⁻¹ potassium as promoters. The iron catalyst supports included cerium and zirconium metallosilicates and Catalox and Dispal commercial aluminum oxides from Sasol. At 325 °C and 20 bar, CO conversion over the Fe/Ce/SiO₂-K,Cu, exceeded 85% while at the same conditions it was only 68% over the unpromoted catalyst. Fe/Zr/SiO₂-K,Cu converted less CO than the cerium-silicate (75%) but the unpromoted zirconium-silicate only converted 43% of the CO. The conversion and selectivity of the Catalox was about the same as the cerium-silicate, while the Dispal performance was equivalent to the zirconium-silicate. This study also highlights the importance of support and promoters in FTS, demonstrates the potential of the NHSG method to synthesize promoted iron catalysts with various supports and lays the foundation for developing efficient and stable catalysts for converting syngas to hydrocarbons.

Keywords: Fischer-Tropsch, Fe catalyst, metallosilicates, promoters,

*Corresponding author

Email address: nazmiye-tugce.eran@polymtl.ca (Tugce N. Eran*)

1. Introduction

As society adopts alternative energy sources to meet industrial and residential needs, several hard to convert sectors like shipping, jet fuel, and long haul trucking will continue to rely on diesel fuel. Biomass, wasted natural gas (flared, bio-gas, landfill gas), and anthropogenic atmospheric CO₂ are green alternatives to petroleum as a bridge-solution for these sectors in which the carbon is converted to CO and reacts with H₂ over Co or Fe catalyst—Fischer-Tropsch synthesis (FTS). Fischer Tropsch synthesis (FTS) was developed one-hundred years ago and is now a corner-stone of gas-to-liquid processes with feedstocks like coal, natural gas, biomass, and even anthropogenic CO₂. In the latter case, CO₂ is converted to CO via the reverse water gas shift reaction. FTS is a more sustainable and environmentally friendly energy vector. The main objectives of FTS studies are principally to identify the optimal combination of catalyst structure and operating conditions to maximize C₅₊ hydrocarbon selectivity and CO conversion [1, 2, 3, 4, 5]. Here we developed and compared various supports for promoted iron catalysts. We also examined the impact of a non-hydrolytic sol-gel method with various promoters. Comparing the promoted and un-promoted iron based catalyst activity on Fischer Tropsch synthesis has been extensively studied and documented [6, 7, 8, 9, 10, 11]. Group 1A alkali metals, especially K, are common and efficient promoters for iron. Potassium increases the average molecular weight of the hydrocarbon products, as reported, for example, in a study with a fixed bed operating at 14.8 bar, 235 °C < T < 265 °C at a syngas ratio H₂:CO=1 [12] Even though copper has a similar effect on the hydrocarbon selectivity, it slightly increases secondary reactions towards alcohols and olefins. Adding both promoters improved FTS and maintains stability for 200 h compared to a single promoted catalyst [13]. Potassium donates electrons to iron, which facilitates CO chemisorption. When H₂ covers the surface, it donates electrons to iron as well, but having an alkali metal (electron donating

K) lowers the electron affinity of H_2 , which weakens the Fe-H bond [14]. This
30 phenomenon decreases the H_2 chemisorption while promoting CO chemisorption
[14]. Metal-carbon bond strength increases while carbon-oxygen bond strength
decreases, which makes it easier for hydrogen to remove oxygen and increase the
FTS reaction rate. Potassium promotion prevents iron reduction, which means
that catalyst needs more time to reach steady-state. Copper facilitates iron re-
35 duction from Fe_2O_3 to Fe_3O_4 , which accelerates the time to reach steady-state
and further boosts the heavy hydrocarbon fraction. Cu-K promotes the forma-
tion of oxygen deficient iron oxide species and eventually reduces the Fe oxide
crystallite size while forming carbides during the activation [15]. Even though
Cu increases the tendency to form CH_4 , K mitigates this trend.

40 Promoter loading also changes the structure and activity of the catalyst and
FTS rate. For a Fe/Cu/SiO₂ catalyst, the Fe-O-Si interaction weakens as the
K loading increases up to 7% [16]. The relationship between catalyst perfor-
mance and loading also depends on catalyst structure, active phase loading,
crystallinity, type of support, feed composition, temperature and pressure. In
45 our previous study, we developed a non-hydrolytic sol-gel (NHSG) method to
prepare metallosilicate supported iron catalysts [17]. The advantages of sol-
gel chemistry include high purity, ability to control the structure, texture, and
homogeneity [18, 19] when applied for the synthesis of FT catalysts. Sol-gel
chemistry depends on multiple factors such as temperature, solvent, aging and
50 drying conditions, water content, and the nature of the precursors. The main
problem with conventional sol-gel methods is the variation of reaction rates for
different mixed oxide precursors. Hydrolysis and condensation rate of each pre-
cursor impacts the homogeneity directly. Another issue is the presence of water,
with the accompanying capillary forces, which collapse the pore network, so an
55 extra step is necessary such as supercritical drying, solvent exchange and/or
applying a templating agent [20, 21, 22, 23]. In conventional NHSG techniques,
metal chloride precursors react with primary and secondary alcohols to form
metal alkoxide. The alkoxides continue to react with metal chlorides. Another
recipe applies tertiary and benzylic alcohols but the catalyst structure with this

60 route is hard to control. The disadvantage of using metal alkoxide precursors is
the high reaction temperature (200 °C to 250 °C) [24, 25]. In our study, we chose
to use a simple and commonly available material, iron nitrate, as a precursor to
synthesize the catalysts. Based on the high CO conversion and HC selectivity
observed in our previous study, we believe that further investigation into the
65 reaction route and kinetics with nitrates in non-hydrolytic sol-gel method is an
interesting topic, seldom investigated in FTS devoted literature. Four differ-
ent catalysts were prepared by NHSG method and studied in this paper. Two
samples were synthesized by preparing metallosilicate supports based on Ce or
Zr and then by adding iron and promoters (K,Cu). Another two samples were
70 synthesized with the same methodology over Catalox and Dispall commercial
supports from Sasol. The goal of the preparation of these last two samples is
to compare homemade metallosilicate supported catalysts with industrial sup-
ports. This exercise provides a universal reference, very rare in the FT scientific
literature, so that other might benchmark their catalyst. For the reason of in-
75 dustrial secrecy, the characterization data on the catalysts prepared starting
from commercial supports and some aspects of synthesis methodology will be
limited in this article.

In summary, the four catalysts investigated in the present work are: (1)
Fe/Ce/SiO₂-K,Cu (2) Fe/Zr/SiO₂-K,Cu (3) Fe/Catalox-K,Cu (4) Fe/Dispall-K,Cu
80 all prepared by NHSG methods. The results for the samples (1) and (2) can be
directly compared with the data published in [17] for the same catalysts in the
absence of K and Cu promoters.

The catalysts were fully characterized and tested in FTS in terms of CO
conversion and product selectivity (CO₂, CH₄, hydrocarbons with less than 7
85 carbon atoms, i.e. C₇₋ and hydrocarbons with 7 or more carbon atoms, i.e.
C₇₊) using syngas (H₂/CO mixture) as feeds. We also examined the impact
of NHSG method on aluminum oxide support and compared the characteristic
aspects and catalytic activity.

2. Experimental

90 2.1. Materials

Zirconium(IV) ethoxide (97 %, solid), ammonium cerium(IV) nitrate (\geq 99.99 %, trace metal basis), iron nitrate nonahydrate (98 %, bioreagent) tetraethyl orthosilicate (TEOS, \geq 99.0 %), tetraethylammonium hydroxide solution (TEAOH, 35 % in aqueous solution), potassium nitrate (ReagentPlus \geq 99.0 %), and copper(II) acetate mono hydrate (ACS reagent, \geq 98 %) were procured from Aldrich and
95 used as received. The structure directing agent, triethanolamine (TEA, \geq 99 %), pluronic P123 (block polymer-poly(ethylene glycol)- block-poly(propylene glycol)- block- poly(ethylene glycol)) were procured from Aldrich. Reagent alcohol (90.2 % ethanol, balance methanol and iso-propanol) was purchased from LabChem,
100 UN1987). Dispal $\text{\textcircled{R}}$ T 25N4-80 (boehmite) Alumina and Catalox $\text{\textcircled{R}}$ SCCa 5/110 Alumina oxides were both acquired from Sasol Chemicals (USA) LLC.

2.2. Support Synthesis

We synthesized the supports based on previous literature [17]. TEOS was mixed with metal precursors (1:10 molar M_xO_y : SiO_2) and stirred for 30 min.
105 Then TEA (mesopore directing agent) was added to this solution and mixed another 30 min. Later the water was added drop wise and the solution was stirred another 60 min. Finally, TEAOH was added to the mixture and the solution was left to age for 24 h. The molar ratio of the resulting gel was 1 SiO_2 :0.1 M_xO_y : 0.3 TEA:0.1 TEAOH:11 H_2O , where M is Ce or Zr based on
110 the choice of the support. We dried the resulting gel at 100 °C for 24 h and calcined it for 10 h at 700 °C.

2.3. Catalyst preparation

We used the same non-hydrolytic sol-gel synthesis method as a previous study [17]. The ethanol (25 mL) and block copolymer P123 (1.8 g) were mixed
115 until the template is homogeneous (40 min to 45 min). Then supports (Catalox, Dispal or metallosilicate, 3 g) and 0.10 g g^{-1} iron nitrate nonahydrate

were added to this solution slowly. To improve the homogeneity, we mixed the solution for 30 min at 40 °C then we added the K (potassium nitrate) and Cu (copper(II) acetate mono hydrate) precursors. We used 0.020 g g⁻¹ K and 0.038 g g⁻¹ Cu as a promoter. After adding the promoters, we continued mixing for 20 min at 40 °C. Later, the final solution was placed into a petri dish and left to gel in the oven at 40 °C with relative humidity of 50 %. The gel aged for 5 days and we collected the catalyst which at this stage was still partially humid due to the moisture retained in the gelation process. The same procedure of drying and calcining of supports was followed for all 4 catalysts. The collected particles dried at 100 °C for 24 h and calcined at 700 °C for 10 h with a heating rate of 1 °C/min in air.

2.4. Characterization

The following instruments were applied to characterize the catalyst samples: LEO 1525 ZEISS (Jena, Germany) SEM evaluated the morphology of the samples [17]. Field emission scanning electron microscopy was applied at an accelerating voltage of 15 kV for 2 min. A Bruker Quantax EDX instrument coupled to the SEM mapped the surface elemental distribution.

The SEM was a JEOL JSM-7600F with a field emission gun (FEG) and a maximum resolution of 1.0 nm at 15 kV. Images can be acquired in both secondary electrons (topographic contrast) and backscattered electrons (chemical contrast). It is equipped with an Oxford X-Max N EDS detector which has an active area of 80 mm² and a spectral resolution of 123 eV at 5.9 keV .

Micromeritics (Tristar II 3020) determined the Brunauer-Emmett-Teller (BET) specific surface area of the samples and measured the adsorption/desorption isotherms from N₂ at -196 °C. The Barrett-Joyner-Halenda (BJH) method was applied to determine the porosity distribution. To remove the contaminants and adsorbed water, the samples were pre-treated at 150 °C under He flow for 4 h.

A Philips PW1710 diffractometer generated the X-Ray powder diffraction (XRD) patterns. The CuK_α radiation was performed with the operating condi-

tions set at 40 kV and 20 mA. The step scan rate was maintained at 1 °C/ min and a counting time 1 s per step was applied. The 2α range spanned from 0° to 90°.

150 D8 Advance Plus Bruker X-Ray Diffraction analyzed the crystallinity of the materials. The X-ray generator was set to 40 kV and 40 mA.

X-ray photoelectron spectroscopy (XPS) analysis was performed using an Escalab 250Xi (Thermo Fisher Scientific) with a monochromated Al K α source at a power of 218.8 W (14.7 kV, 14.9 mA), a 180°, double-focusing, bipolar hemi-
155 spherical analyzer, and standard charge compensation using low energy electrons and Ar⁺. The pressure in the analysis chamber during the measurement was kept below 2×10^{-7} mbar. Survey spectra were acquired at a pass energy of 150 eV and a step size of 1.0 eV. High resolution spectra were acquired at 20 eV pass energy and a step size 0.1 eV. This yields a FWHM for the ester peak in
160 polyethylene terephthalate (PET) of 0.81 eV. Based on typical values for electron attenuation length this yields an XPS analysis depth of 5 nm to 10 nm for a flat surface. Data processing was performed using Advantage v6.5.0 (Thermo Fisher Scientific). All elements present on the surface (except H and He which are not detected by XPS) were identified from survey spectra. Their atomic
165 concentrations were calculated using integral peak intensities and the sensitivity factors supplied by the manufacturer. Binding energies were referenced to the C1s peak at 285.0 eV for aliphatic hydrocarbons.

2.5. FT bench scale reactor

The catalysts were tested using the same apparatus as in a previous work
170 [17]. CO, H₂, N₂ (as internal analytical standard) were regulated by Brooks flowmeters and fed to the fixed bed reactor. The catalysts were placed, without dilution, in a 6 mm internal diameter packed bed and a GHSV=2805 h⁻¹. The catalyst bed was held in place with quartz wool. A K-type thermocouple measured the temperature inside the catalytic bed. To activate the catalyst,
175 we introduced a mixture of H₂ and CO (in a 2:1 molar ratio) with a flow rate of 53 NmL/ min, while maintaining the temperature at 350 °C and pressure at

20 bar for a duration of 4 h. We assumed time zero as we reach the required temperature and pressure. After the reactor, a 0.13 L cold trap maintained at 5 °C and 20 bar, collected the condensed reaction products, i.e. water and heavy hydrocarbons liquid. We only collected liquid products from C₅ to C₂₀ in a cold trap while the effluent was monitored by GC [26]. A back pressure regulator maintained the reactor at 20 bar during FT test, after the activation step. An Agilent 3000A micro gas chromatograph analyzed the permanent gases (N₂ and non converted H₂ and CO) and non-condensable hydrocarbons so we determined the CO conversion (X_{CO}) based on N₂ and CO peak areas (A_{N_2} and A_{CO}) their relative response factor (k), and inlet (set) flowrate of CO and N₂ (F_{in,N_2} , and $F_{in,CO}$) (Eq. 1). The selectivity of desired product(s) ($S_{product}$) was determined as stated in the Eq 2 [17]. QPLOT columns and molsieves are installed in the instrument. He was the carrier gas and GC oven was maintained the column temperature at 50 °C. The micro GC sampled the effluent every 2 h. To ensure the accuracy and reliability of the experimental data, detailed carbon mass balance calculations were conducted for the FTS experiments. These calculations involved quantifying the input moles of carbon from CO and the output moles from all produced hydrocarbons and unreacted CO. The analysis indicated that the carbon balance error for each of the four catalysts tested remained below 5 %. This result confirms the fidelity of the experimental data, accurately reflecting the catalysts' performance in the conditions tested. We determined the alpha (α) values, representing the probability of chain growth during Fischer-Tropsch synthesis, using the Anderson-Schulz-Flory distribution model (Eq 3) (Eq 4) where W_n is the mole fraction of a hydrocarbon with chain length n , n is total carbon atom number, α is the probability of chain growth ($\alpha < 1$) and $(1-\alpha)$ is the probability of chain terminations [27]. This model is pivotal for predicting the distribution of hydrocarbon chain lengths produced in FTS, offering insights into the efficiency and selectivity of the catalysts under study.

$$X_{\text{CO}} = \frac{F_{\text{in, CO}} - F_{\text{in, N}_2} \cdot k \cdot \frac{A_{\text{CO}}}{A_{\text{N}_2}}}{F_{\text{in, CO}}} * 100 \quad (1)$$

$$S_{\text{product}} = \frac{\text{moles of desired product(s)}}{\text{moles of CO}_{\text{in}} - \text{moles of CO}_{\text{out}}} * 100 \quad (2)$$

$$\frac{W_n}{n} = (1 - \alpha) \cdot \alpha^{(n-1)} \quad (3)$$

$$\ln(\alpha) = n \ln(\alpha) + \ln \left[\frac{(1 - \alpha)^2}{\alpha} \right] \quad (4)$$

3. Results and Discussion

3.1. Characterization

SEM-EDS analysis identified Fe, Ce, Si, K and Cu in blue, cyan, magenta,
 210 green and yellow, respectively (Figure 1) for the Fe/Ce/SiO₂-K,Cu catalyst.
 Based on the brightness of the images, Ce is the most well distributed on the
 surface. Fe and Si were distributed fairly well but some of the iron particles
 are embedded inside of the matrix. There were few islands of iron particles on
 the surface but they were mostly located below the cerium. Si particles were
 215 both located on the surface and in the core most likely. Si has a tendency to
 make weak connections with iron. So, it is possible that Fe is located around
 the Si [28, 29]. K and Cu promoters on the other hand, were homogeneously
 distributed. However, since their mass loading is quite low, the images appear
 darker compared to the rest of the elements. The mixed image also showed
 220 that cerium was mostly distributed on the surface of the catalyst while silica
 appeared more as small islands on the surface. We detected iron species more
 clearly but it is clouded by the presence of other elements.

SEM images for Fe/Zr/SiO₂-K,Cu demonstrated Fe, Zr, Si, K and Cu in
 blue, yellow, magenta, orange and green respectively (Figure 2). The iron par-
 225 ticles were located predominantly on the zirconium silica supported catalyst

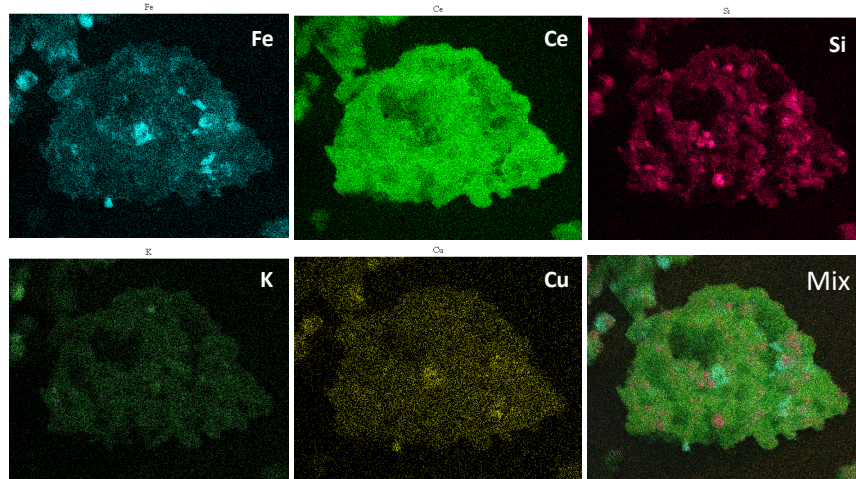


Figure 1: Detailed SEM-EDX representation of Fe/Ce/SiO₂-K,Cu and mix of all the elements, x750 magnification, 10 μm scale

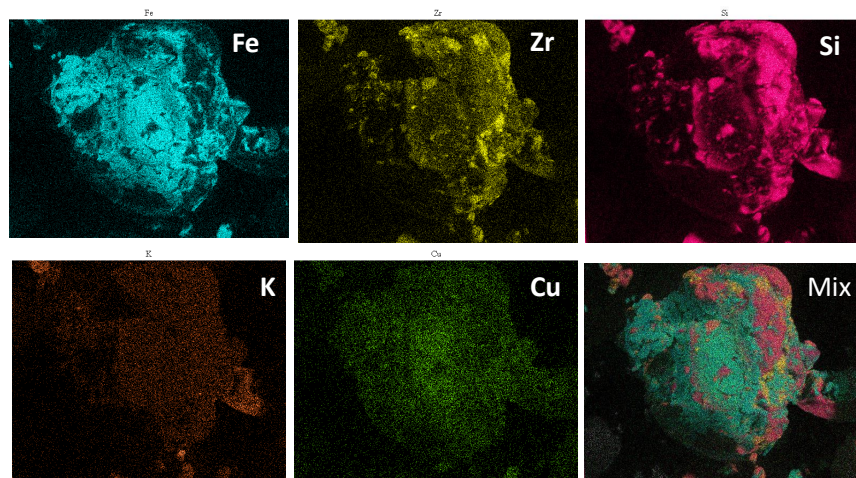


Figure 2: Detailed SEM-EDX representation of Fe/Zr/SiO₂-K,Cu and mix of all the elements, x270 magnification, 10 μm scale

surface and their distribution were more homogeneous compared to cerium silicate supported catalyst. Si was more heterogeneously distributed on the surface. K and Cu behaves similarly in both catalysts and distributed relatively homogeneously and located mostly below the surface of the catalyst. Also, SEM analysis is conducted on a limited number of spots, which may not accurately represent the entire structure of the catalyst.

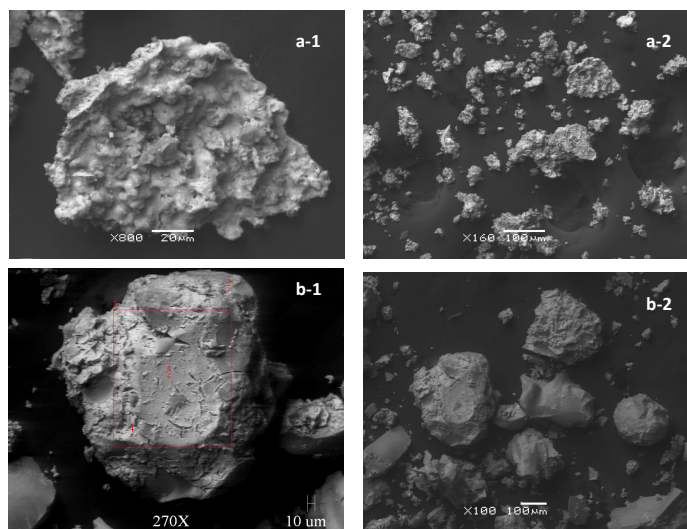


Figure 3: The Scanning Electron Microscope Images of both Fe/Ce/SiO₂-K,Cu (a-1: x800 and a-2: x160 magnification) and Fe/Zr/SiO₂-K,Cu (b-1: x270 and b-2: x100 magnification)

Compared to the non-promoted catalysts [17], both metallocate supported catalysts are less porous and more rigid (Figure 3). Non-promoted catalysts had a sponge like structure that facilitates the flow of reactants through the openings, mostly for Fe/Ce/SiO₂ rather than Fe/Zr/SiO₂ catalyst [17]. The extra metal deposition (promoter addition) on the catalyst surface fills the porous structure of the catalyst and narrows the pores (Figure 3,b-1 and b-2) [30]. For the Fe/Ce/SiO₂-K,Cu catalyst, pores might have turned into cavities because the surface was still more rough than Fe/Zr/SiO₂-K,Cu. The surface of Fe/Zr/SiO₂-K,Cu had small cracks due to capillary forces or high temperature

in the calcination stage. The particle size for Fe/Ce/SiO₂-K,Cu was around 115 μm while it was 110 μm for Fe/Zr/SiO₂-K,Cu (Table 1).

Table 1: Different properties of iron supported catalysts

Catalysts	Particle diameter (μm)	Average Pore diameter (nm)	Pore volume (cm ³ g ⁻¹)	Specific surface area (m ² g ⁻¹)	d (Fe ₂ O ₃) (nm)	d (Fe ₃ O ₄) (nm)
Fe/Ce/SiO ₂ -K,Cu	115	16	0.1	24	9	-
Fe/Zr/SiO ₂ -K,Cu	110	4	0.1	204	2	-
Fe/Catalox-K,Cu	64	6	0.4	84	6	-
Fe/Dispall-K,Cu	50	6	1.0	150	-	3

The catalysts containing the Sasol support, Fe/Catalox-K,Cu and Fe/Dispall-K,Cu were predominantly spherical (Figures 4bc, 5bc) with some donuts (Figures 4a,5ab). The Catalox as a support had the same spherical shape as the catalyst according to the Sasol technical sheet. This suggests that, the NHSG method preserves the shape and structure of the original precursor and it is a non-invasive method. However, created colloidal structure still managed to hold the additional metal oxide on the surface. SEM-EDX indicated that iron particles formed few islands on the surface around the support. Al, Cu, and K are distributed relatively evenly (Supporting Document 5a). There are a few iron and potassium particles located inside of voids. For the Dispall supported catalyst, the metal distribution is similar, however, the spot analysis indicated that Fe, K, and Cu weight percent average is 5% lower than the Catalox supported catalyst. The common detail about these both catalysts is that higher Al content on the catalyst surface compared to Si of metallosilicates. (Supporting Document 5ab)

The BET surface area of Fe/Ce/SiO₂-K,Cu and Fe/Zr/SiO₂-K,Cu were lower than the non-promoted catalysts: 24 m² g⁻¹ for Fe/Ce/SiO₂-K,Cu and

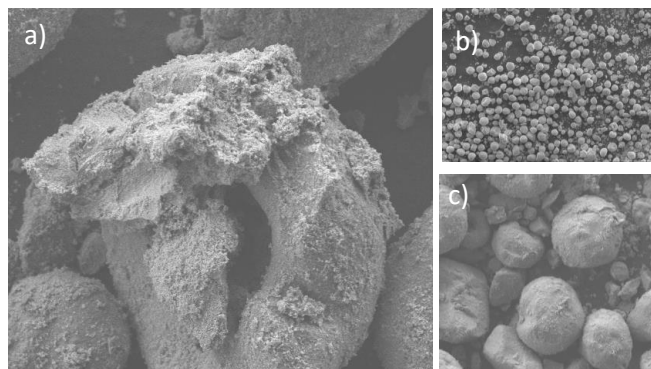


Figure 4: SEM of Fe/Catalox-K,Cu (a) x1400, (b) x65 and (c) x1000 magnification

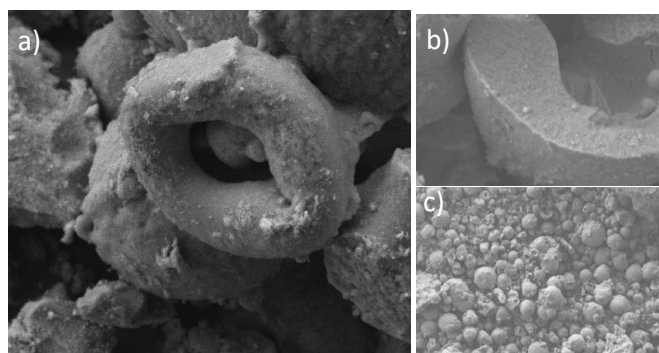


Figure 5: SEM of Fe/Dispall-K,Cu (a) x3500 (b)x5000 (c) x250 magnification

260 $204 \text{ m}^2 \text{ g}^{-1}$ for Fe/Zr/SiO₂-K,Cu for fresh catalysts (Table 1). The disparity
in surface area between these two catalysts primarily stems from the impact of
precursor used in the sol-gel method for synthesizing the supports. We synthe-
sized the supports using the conventional sol-gel method, which utilizes water
as a solvent. This method is influenced by factors such as the type of precursor,
265 water content, pH of the solution, and temperature of the reaction [31, 32, 33].
Conventional sol-gel method (water as a solvent) used in the support synthesis
is sensitive to the type of precursor due to different hydrolysis and condensation
rates during the reaction. Apart from the precursor type, we prepared both sup-
ports simultaneously under the identical conditions. Despite having the same
270 metal loading for the ammonium cerium nitrate and zirconium ethoxide precu-
sors, the surface areas differed by an order of magnitude. A similar conventional
sol-gel method [34] also reported large differences in BET surface area of the
supports: $42 \text{ m}^2 \text{ g}^{-1}$ for cerium silicate support and $366 \text{ m}^2 \text{ g}^{-1}$ for zirconium
silicate support [17]. The influence of different precursors on surface area can
275 also be observed in the referenced study, where the researchers synthesized Al,
Ti, Zr, Ce, V, and Zr metallosilicates with cobalt as an active phase for FTS
[34]. The surface area of these supports ranged from $16 \text{ m}^2 \text{ g}^{-1}$ (for vanadium
silicate synthesized using ammonium metavanadate) to $627 \text{ m}^2 \text{ g}^{-1}$ (for titanium
silicate synthesized using titanium n-butoxide). Moreover, the BET results from
280 that study demonstrated a $217 \text{ m}^2 \text{ g}^{-1}$ difference in surface area between cerium
silicate and zirconium silicate supports [34].

We measured the surface area for fresh catalyst and after 90 h reaction with
syngas ($\text{H}_2/\text{CO}=2$) at 20 bar and 275 °C to 325 °C. Both Fe/Ce/SiO₂-K,Cu
and Fe/Zr/SiO₂-K,Cu catalysts had a mesoporous structure, which was main-
285 tained after reaction. The nitrogen adsorption-desorption for Fe/Ce/SiO₂-K,Cu
resembles Type III isotherms with a H3 hysteresis loop. This is typical of
non-rigid aggregates of clay type, plate-like particles [35, 36, 37]. After reac-
tion, the pores are narrower because of the carbon deposition (Figure 6). The
isotherms of the fresh Fe/Zr/SiO₂-K,Cu resembles a H5 hysteresis loop of a
290 Type IV adsorption-desorption isotherms, which is linked with partially open

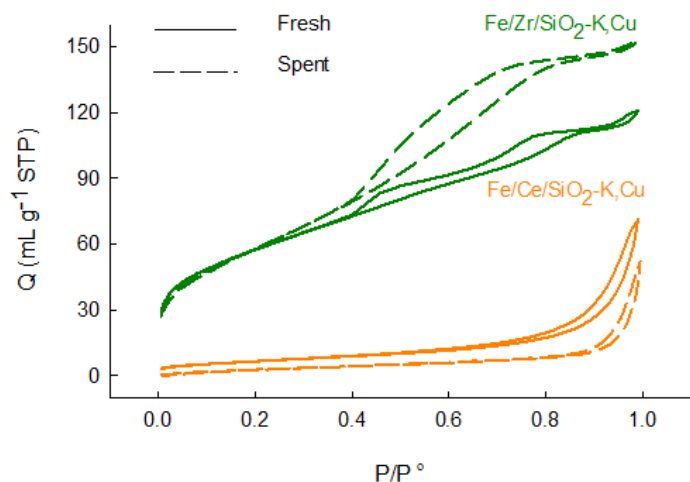


Figure 6: BET adsorption-desorption isotherms of both Fe/Ce/SiO₂-K,Cu and Fe/Zr/SiO₂-K,Cu fresh and spent

pore structures containing cylindrical mesopores (Figure 6). After the reaction it had Type IV isotherms with a H2(a) hysteresis loop that is associated with bottle-neck looking pores characteristic of many silica gels, porous glasses, and mesoporous materials [37]. The interaction of gas through the partially open pores enlarges the mouth of the pores. This also explains why the pore size and BET surface area is larger after the reaction ($207 \text{ m}^2 \text{ g}^{-1}$). Since the zirconium silicate supported catalysts were less active, the carbon deposition on the pores could have less impact on the pore size as well. Pore size distribution demonstrated that most pore sizes are in between 2 nm to 5 nm indicating mesoporous structure with 44% and 84% for cerium and zirconium supported iron catalyst, respectively (Figure 7).

The BET surface area was $84 \text{ m}^2 \text{ g}^{-1}$ for the Catalox supported catalyst and $150 \text{ m}^2 \text{ g}^{-1}$ for the Dispal supported catalyst. They both had about the same pore size (6 nm) and a mesoporous structure. Based on their pore size distribution, the highest percentage is in between 2 nm to 5 nm for sasol supported catalysts as well with 64% and 56% for Fe/Dispal-K,Cu and Fe/Catalox-K,Cu

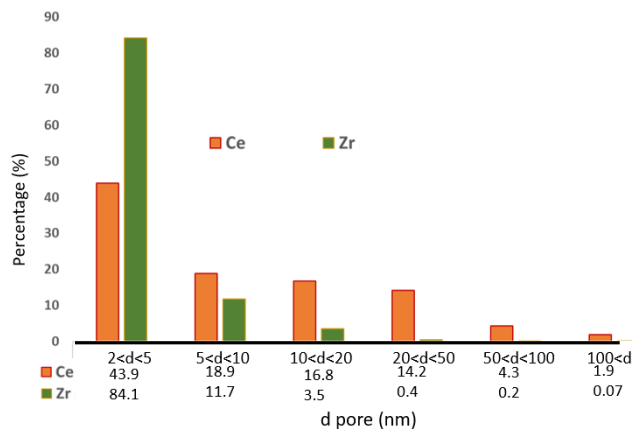


Figure 7: The pore size distributions from $d < 2$ nm and $100 \text{ nm} < d$ for Fe/Ce/SiO₂-K,Cu-orange and Fe/Zr/SiO₂-K,Cu-green.

respectively (Figure 8). The particle size for Fe/Catalox-K,Cu was around 64 μm while it was 50 μm for Fe/Dispall-K,Cu (Table 1) .

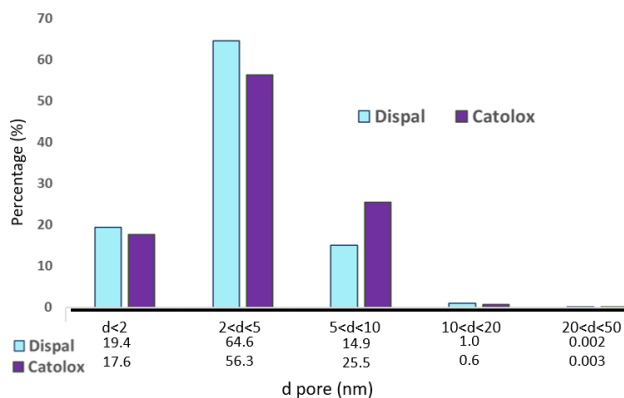


Figure 8: The pore size distributions from $d < 2$ nm and $100 \text{ nm} < d$ for Fe/Catalox-K,Cu-purple, Fe/Dispall-K,Cu-turquoise

The Fe/Catalox-K,Cu follows a Type V adsorption-desorption isotherm which
 310 was similar to zirconium silicate supported catalysts that indicate molecular
 clustering, partially-open ordered pores (Figure 9). This is common for meso-

porous structures, mixed oxides, and xerogels. The hysteresis loops were close to H2(a)—bottle neck structured pores. H2 type loops are common for silicate/aluminosilicate pore structures. The Fe/Dispall-K,Cu catalyst had Type III isotherm and similar to Type V as well with the H3 type hysteresis loop. For the H3 loop, the pore structure is ill defined [38, 39, 37].

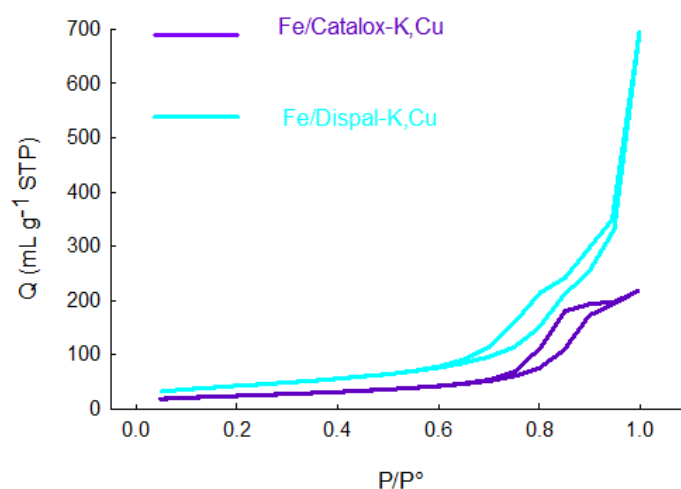


Figure 9: BET adsorption-desorption isotherms of both Fe/Catalox-K,Cu and Fe/Dispall-K,Cu

The XRD diffractograms of the samples (Figure 10 and Figure 11) were interpreted with both EXPO2014 and the Match! software. Since both metallosilicate supported catalysts include multiple metal oxides, the patterns overlap [40]. The Match software computes and matches the peaks along with the amounts and phases of the elements based on COD (Crystallography Open Database) where EXPO2014 solves crystal structures (if there is any) by powder diffraction data by using reciprocal as well as direct space methods. According to the software, the Fe/Ce/SiO₂-K,Cu identified Fe₂O₃-hematite as the Fe phase and the peak values are confirmed by other studies [41, 42, 43, 44]. The software identified SiO₂ and CeO₂ along with K₂O and the tenorite form of CuO

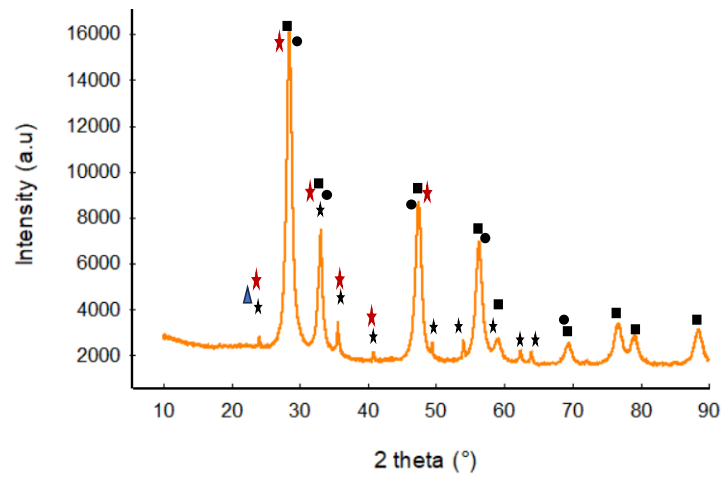


Figure 10: X-Ray Diffractograms of both Fe/Ce/SiO₂-K,Cu black star-Fe₂O₃, black square CeO₂, black circle - CuO, red star-K₂O, blue circle- SiO₂

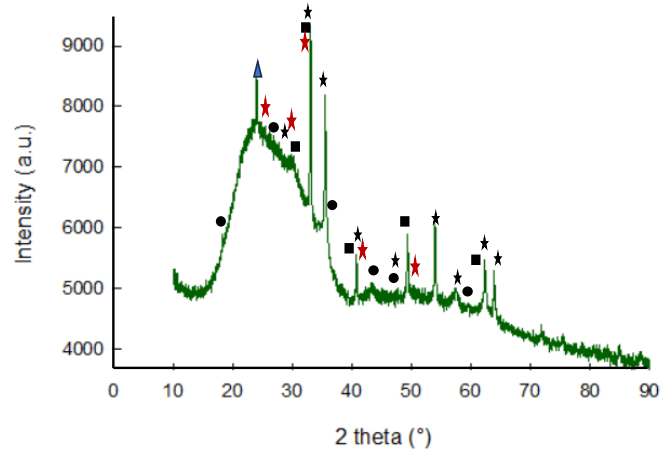


Figure 11: X-Ray Diffractograms of both Fe/Zr/SiO₂-K,Cu black star-Fe₂O₃, black square ZrO₂, black circle - Cu₃O₄, red star-K₂O, blue triangle- SiO₂

(Figure 10). The Fe/Zr/SiO₂-K,Cu displayed peaks characteristic of Fe₂O₃ in hematite form [43, 44]. The analyses were based on ICDD and COD, which identified in its crystalline structure, the Fe/Zr/SiO₂-K,Cu catalyst has the
330 paramelaconite form of Cu₄O₃ along with ortho I phase of ZrO₂ (Figure 11). In addition to this, there are SiO₂ peaks in mutinaite phase. Since the software assigned a value of 76 % to SiO₂, it is likely that the Fe/Zr/SiO₂-K,Cu is amorphous. This is further evidenced by the presence of a “hump” on the baseline of its diffractograms [45].

335 We observed some residual structures of CeSiO₂ and ZrSiO₄ originated from the support material for Fe/Ce/SiO₂-K,Cu and Fe/Zr/SiO₂-K,Cu, respectively. This also suggests that we successfully synthesized cerium silicate and zirconium silicate supports separately. EXPO2014 software analysis also confirmed this finding. From the XRD results of Fe/Ce/SiO₂-K,Cu, we differentiate the neat
340 peaks which represents crystallinity. EXPO2014 was able to form a crystalline structure for Fe/Ce/SiO₂-K,Cu (Figure 12), unlike for Fe/Zr/SiO₂-K,Cu due to its amorphous structure [46, 47, 48, 44, 49, 43, 50, 51]

For the Catalox supported catalyst, the Fe₂O₃-hematite appeared as the active phase while for the Dispal supported catalyst, the iron phase was Fe₃O₄
345 based on the XRD results. However, for the Fe/Catalox-K,Cu, a small trace of Fe₃O₄ was also present. In Fe/Catalox-K,Cu, the XRD has a K₂O peak and we were also able to identify small percentage of AlKO₂ (Figure 13 and Figure 14), which suggests a bond bridge between the support and the promoter. The Cu₄O₃ was tetragonal and Al₂O₃ in theta form. The Fe/Dispal-K,Cu consisted of iron oxide as magnetite, Fe₃O₄, and Al₂O₃, CuO in tenorite form,
350 with a trace of KO₃. However, the peaks in Dispal supported catalyst was not as sharp as the Catalox supported catalyst, which could be the reason why the latter was more stable and active. This suggests that Fe/Dispal-K,Cu consists of an amorphous aluminum oxide structure that is similar to zirconium
355 silicate supported catalyst (Supporting Figure 1-4). Especially iron crystallite size correlate with CO conversion and C₅₊ product selectivity. In our case, iron crystallites between 6 nm to 10 nm are more active and produce a heavier hydro-

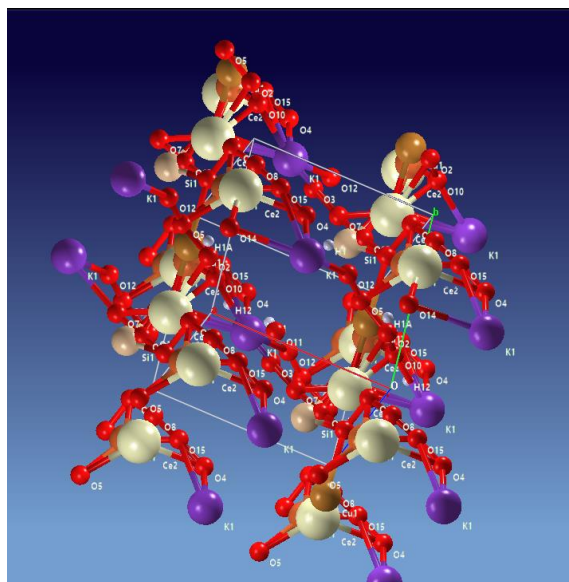


Figure 12: Crystalline structure of Fe/Ce/SiO₂-K,Cu according to analysis of XRD data by the EXPO2014 software

carbons (Table 1). The crystallite size smaller than 6 nm to 12 nm demonstrates lower catalytic activity, higher methane and CO₂ selectivity and lower the chain growth. [52, 53, 54].

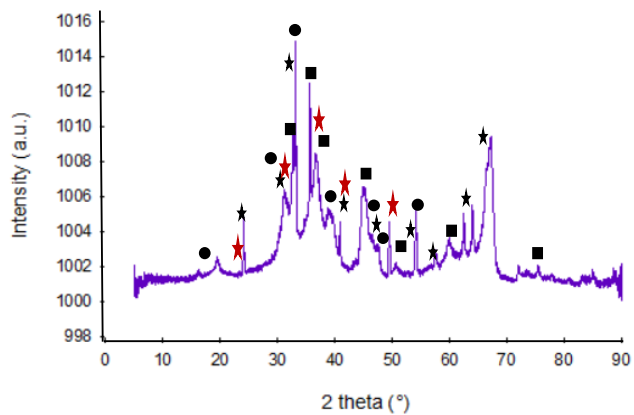


Figure 13: XRD of Fe/Catalox-K,Cu and black star—Fe₂O₃, black square Al₂O₃, black circle—Cu₃O₄, red star-K₂O

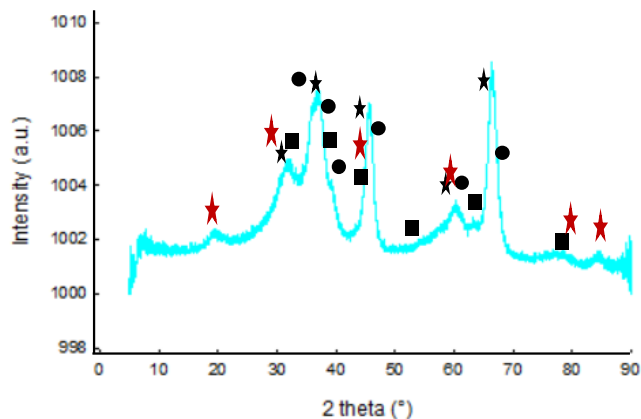


Figure 14: X-Ray Diffraction of both Fe/Dispal-K,Cu and black star— Fe_3O_4 , black square Al_2O_3 , black circle— CuO , red star— KO_3

Both catalysts have mixed oxides which appears at the same 2θ °. For example, Fe_2O_3 [43], Fe_3O_4 [55], K_2O [56], CuO [57, 58], Al_2O_3 [59] and Cu_4O_3 [60] has at least 2 peaks assigned to this crystal structure in between 30-40 2θ °. Therefore, it is challenging to distinguish the peaks and this is why some peaks appear merged. Also similar to metallosilicates, EXPO2014 identified an ordered crystalline form for Catalox supported catalyst but not for the Dispal supported one (Figure 15). Further analysis performed by XPS confirms the oxidation state or chemical state of the metallic elements.

The surface of the sample was gently etched using Ar^+ cluster ions at 4 keV for 1000 atoms clusters to remove adventitious carbon contaminants. All spectra are charge corrected to the remaining C1s peak at a binding energy (BE) of 284.8 eV. The survey spectra obtained from the metallosilicate supported catalysts (Fig 16) displayed the presence of elements Si, K, O, Fe, and Cu, also the corresponding metallic element, Ce or Zr for Fe/Ce/ SiO_2 -K,Cu and Fe/Zr/ SiO_2 -K,Cu catalysts, respectively with the elemental quantification (Table 2). The lower Si concentration and higher concentrations of K, Fe, and Cu observed on the surface of Fe/Ce/ SiO_2 -K,Cu compared to Fe/Zr/ SiO_2 -K,Cu

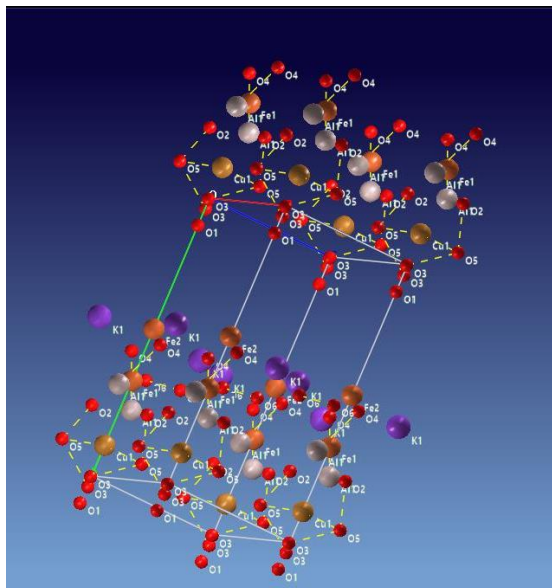


Figure 15: Crystalline structure of Fe/Catalox-K,Cu according to analysis of XRD data by the EXPO2014 software

suggests an increased metal distribution on the SiO₂ support in the Fe/Ce/SiO₂-K,Cu compared to the latter catalyst (Table 3).

380 The high resolution XPS spectra for both Fe/Ce/SiO₂-K,Cu and Fe/Zr/SiO₂-K, Cu (Fig 17) indicated a Si2s peak centered at BE=153.4 eV consistent with Si in silicates, and K2p_{3/2} (K2p_{1/2}) peak at BE=293.6 (295.4) eV, consistent with K bonding to oxygen atoms. The highest intensity of the Fe2p_{3/2} peak was observed at BE=711.4 eV consistent with a dominant presence of Fe in Fe(III) oxide. Fe/Ce/SiO₂-K, Cu also indicated a well-defined Fe2p_{3/2} shake up peak at BE=719.2 eV as expected in Fe(III) oxides. The Fe/Zr/SiO₂-K,Cu exhibited a noticeable broadening of the Fe2p_{3/2} peak towards 708.0 eV, suggesting the existence of a minor concentration of Fe(II) oxide, potentially linked to the presence of magnetite in the sample.

390 For both catalysts, the Cu2p_{3/2} peak had the highest intensity at BE=934.0 eV and indicated intense shake up satellite ranging from 940 eV to 945 eV consistent with Cu in Cu(II) oxide (CuO)[61]. In the Fe/Ce/SiO₂-K, Cu catalyst, the Ce3d

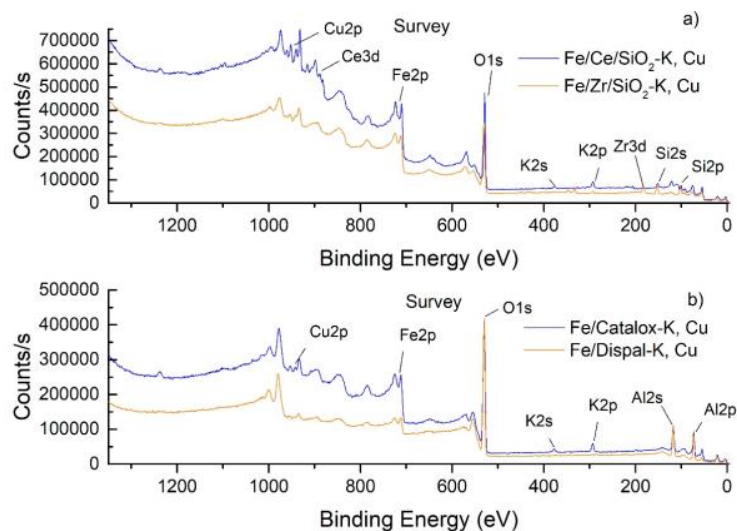


Figure 16: XPS survey spectra for catalysts a) Fe/Ce/SiO₂-K,Cu (blue line) and Fe/Zr/SiO₂-K,Cu (orange line), and b) Fe/Catalox-K,Cu (blue line) and Fe/Dispall-K,Cu (orange line)

Table 2: Elemental quantification table from survey spectra for metasilicate catalysts

Element and orbital	BE (eV)	Relative atomic %	
		Fe/Ce/SiO ₂ -K,Cu	Fe/Zr/SiO ₂ -K,Cu
Si2p	102.4	7.1	17.9
Zr3d	182.7	—	1.8
K2p	294.4	3.1	1.7
O1s	530.9	74.1	68.8
Fe2p _{3/2}	711.4	8.5	7.1
Ce3d _{5/2}	883.2	1.3	—
Cu2p _{3/2}	933.8	6	2.8

Table 3: Metal to Si concentration ratios for metallosilicate catalysts

Species concentration ratio	Fe/Ce/SiO ₂ - K,Cu	Fe/Zr/SiO ₂ - K,Cu
Zr or Ce/Si	0.2	0.1
K/Si	0.4	0.1
Fe/Si	1.2	0.4
Cu/Si	0.9	0.2

spectrum displayed spin-orbit components Ce3d_{5/2} and Ce3d_{3/2} separated by 16.0 eV. Each of these components further splits into three multiplet components, consistent with the presence of CeO₂. The catalyst Fe/Zr/SiO₂-K,Cu: Zr3d was curve-fit using two spin-orbit split ($\Delta=2.4$ eV) doublet Lorentzian/Gaussian (L/G) peaks of fixed relative intensity 2:3 for Zr3d_{3/2}: Zr3d_{5/2} with constant full-width-half-maximum (FWHM) and L/G ratio. Components of Zr3d_{5/2} appearing at BE=181.9 eV and BE=183.2 eV could be related to the presence of ZrO₂ and ZrSiO₄.

Both Sasol supported catalysts demonstrate similar concentrations of Al and O as a percentage in the sample (Fig 16-b) (Table 4 Table 5). The concentration of Fe relative to Al was similar. Concentrations of K and Cu were significantly higher on the surface of Catalox compared to Dispal. The low concentrations of Fe, K and Cu relative to aluminum oxide found for both catalysts indicated that the metals were more homogeneously distributed or embedded in the catalyst body compared to the silicate supported catalysts for which had higher surface concentrations relative to Si. For both cerium and zirconium silicate supported catalysts, the SiO₂ was located below the surface while the other elements were at the surface (Figure 18). These findings were confirmed with SEM-EDS results as well, which helped us deduct the catalyst structure for both iron metallosilicates and iron aluminum oxides [62] (Figure 18). (Figure 1, Figure 2, Supporting Document 5-a, 5-b)

The high resolution spectra for Sasol-supported catalysts (Fig 19) indicated

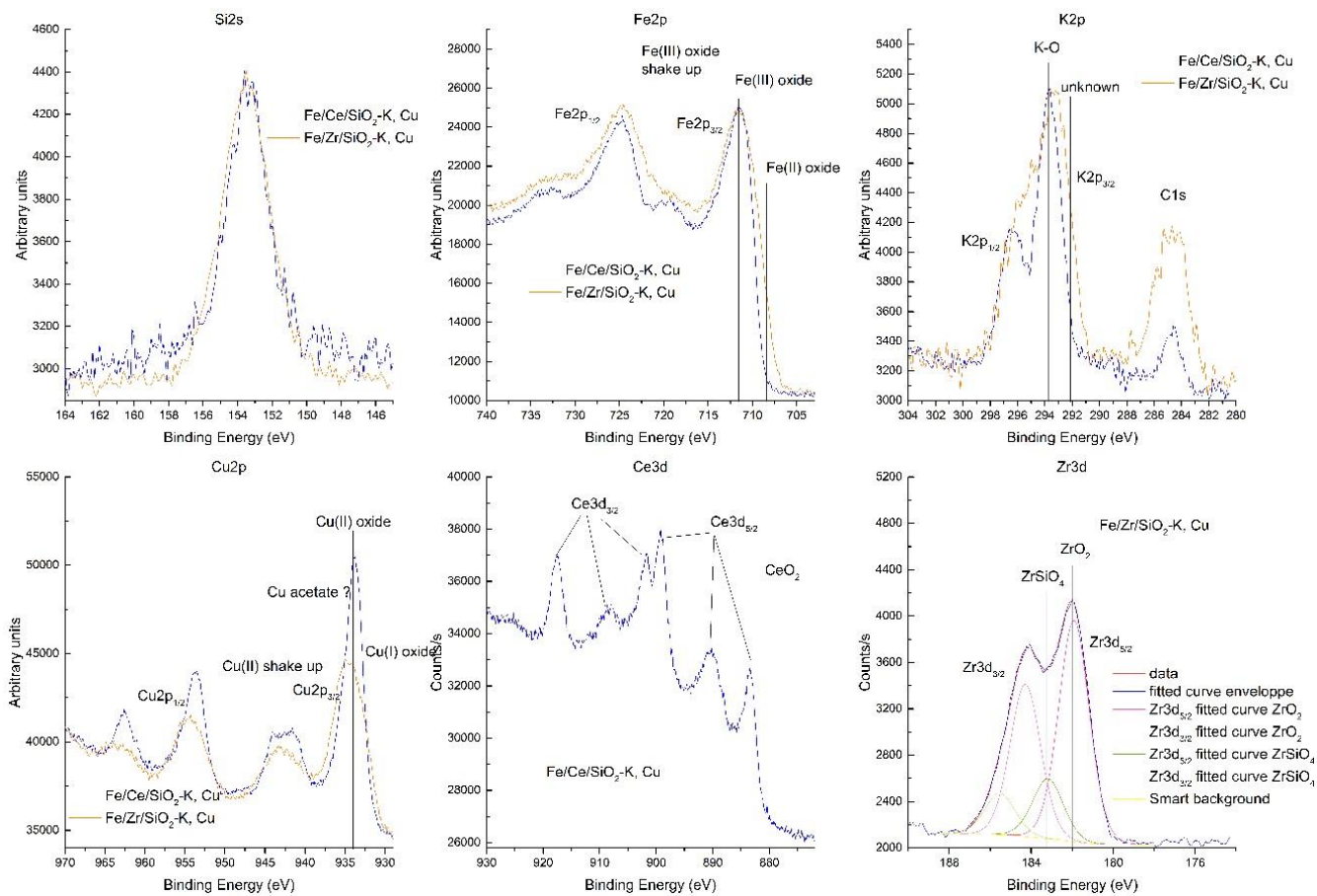


Figure 17: High resolution spectra for catalysts a) Fe/Ce/SiO₂-K,Cu (blue line) and Fe/Zr/SiO₂-K,Cu (orange line). The intensity for spectra Si2s, Fe2p, K2p, and Cu2p was normalized to maximum intensity to ease comparison of spectral shape.

Table 4: Elemental quantification table from survey spectra for aluminum oxide-supported catalysts

Element and orbital	BE (eV)	Relative atomic %	
		Fe/Catalox-K,Cu	Fe/Dispall-K,Cu
Al2p	74.8	34.3	36.1
K2p	295.1	2.2	0.3
O1s	531.9	58.6	60.1
Fe2p3/2	712.4	3.7	3
Cu2p1/2*	955	1.2	0.5

Table 5: Table of metals to Al concentration ratios for aluminum oxide supported catalysts.

Species concentration ratio	Fe/Catalox-K,Cu	Fe/Dispall-K,Cu
K/Al	0.06	0.01
Fe/Al	0.1	0.1
Cu/Al	0.03	0.01

415 Al2s at BE=118.0 eV, which is consistent with Al in alumina. The broader
 peak for Dispal could be indicative of a more disordered structure for this sup-
 port. K2p3/2 was observed at BE=293.0 eV, which is consistent with K in
 metallosilicate-supported catalysts. (Ref. NIST XPS database SRD 20). Fe2p
 had a very similar shape for both Catalox and Dispal supported catalysts, con-
 420 sistent with Fe₂O₃. However, maximum intensity of Fe2p3/2 was found at
 BE=712.0 eV for Fe/Catalox-K,Cu while it was at BE=713.0 eV for Fe/Dispal-
 K,Cu. The shift in binding energy could be due to differences in oxide structure
 or crystallinity. Since XRD indicated that Fe₃O₄ as the dominant iron phase
 in Fe/Dispal-K,Cu with mostly amorphous structure compared to Fe/Catalox-
 425 K,Cu, this is a strong possibility. A similar effect was observed in the Cu2p
 spectra where the lineshapes are consistent with Cu in Cu(II) oxide, but the
 binding energy at which the Cu2p3/2 peaks are observed, 934.4 eV and 935.5 eV
 for the Fe/Catalox-K,Cu and Fe/Dispal-K,Cu respectively, are higher than gen-
 erally observed.

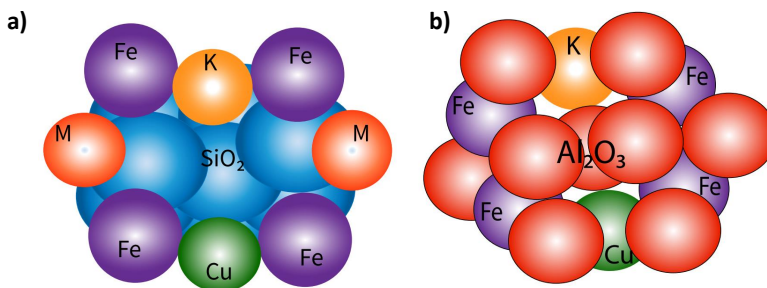


Figure 18: Schematic representation of a) metallosilicate supported and b) aluminum oxide supported iron catalysts

430 *3.2. FT Reaction*

The Fischer Tropsch reaction forms hydrocarbons ranging from C_1 to C_{100} ,
 carbon dioxide, and water. We report CO conversion, and selectivity of CO₂,
 CH₄, light hydrocarbons from C_2 to C_6 and heavy hydrocarbons, C_{7+} . After
 the catalyst was activated at 350 °C for 4 h, the reactor was set at 200 °C and

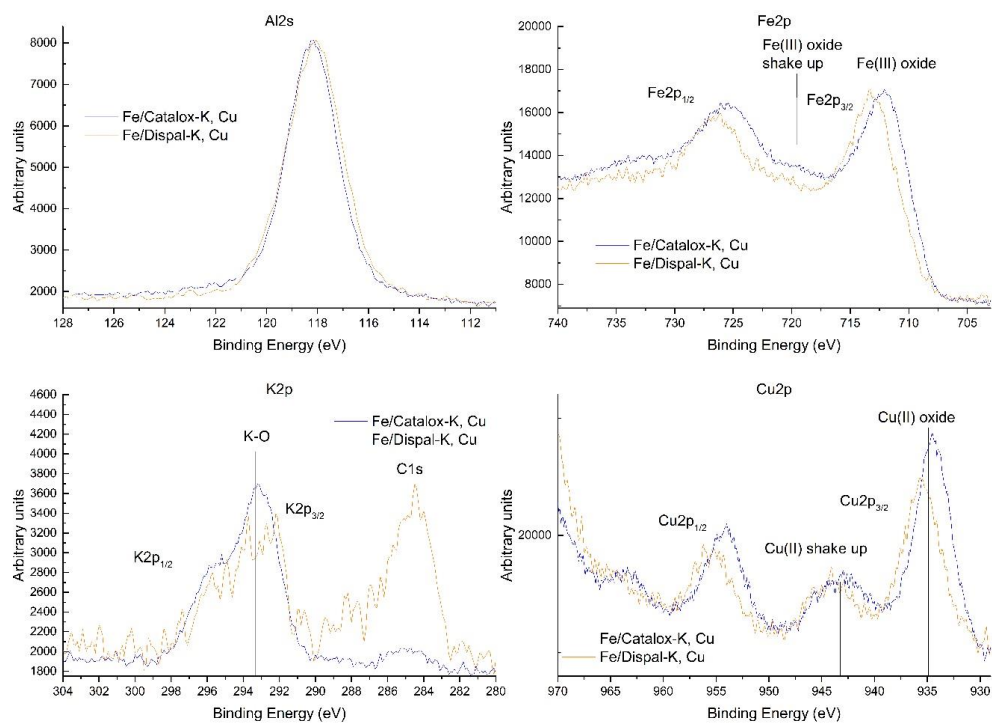


Figure 19: High resolution spectra for catalysts Fe/Catalox-K,Cu (blue) and Fe/Dispal-K, Cu (orange). Spectral intensity was normalized to maximum intensity to ease comparison of spectral shape.

435 ramped every 24 h (220 °C, 250 °C, 275 °C, 300 °C, 325 °C, typically). All the tests were conducted at 20 bar, 200 °C to 350 °C, and a 2:1 H₂/CO molar ratio. Experimental data were recorded after reaching steady state. The CO conversion for Fe/Ce/SiO₂-K,Cu catalysts increased from 13 % at 200 °C, to 48 % at 275 °C, and finally 86 % at 325 °C. (Figure 20). For the Fe/Zr/SiO₂-K,Cu 440 conversion was 10 % at 200 °C, and increased to 40 % at 275 °C and to 76 % at 325 °C. The overall CO conversion for Fe/Ce/SiO₂-K,Cu is higher than the Fe/Zr/SiO₂-K,Cu catalyst but they both follow the same trend with temperature. At a reaction temperature of 350 °C for 30 h, non promoted Fe/Ce/SiO₂ and Fe/Zr/SiO₂ catalysts achieved conversion of only 68 % and 52 % ,respectively [17]. The selectivity of both catalysts followed the same trend with tem-

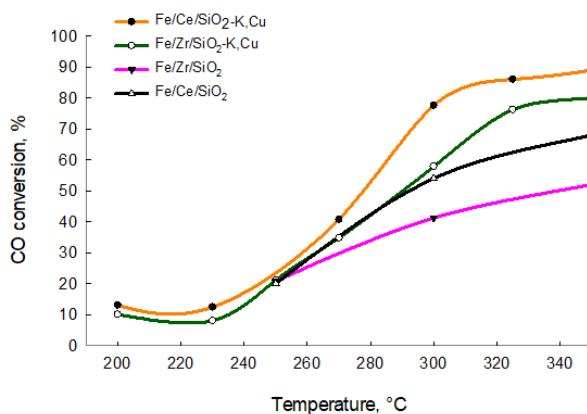


Figure 20: Change in CO conversion with temperature, for Fe/Ce/SiO₂-K,Cu and Fe/Zr/SiO₂-K,Cu with their non promoted versions of each catalysts [17]

445 perature (Figure 21) For the promoted Fe/Ce/SiO₂-K,Cu , CH₄ selectivity is the lowest, starting at around 1 % at 220 °C and then increasing, as expected, reaching a maximum of 13 % at 325 °C. The non-promoted counterparts on the other hand, had the lowest methane selectivity at 250 °C at 6 % but reached 15 % 450 at 270 °C and 27 % at 300 °C. The Fe/Zr/SiO₂-K,Cu overall CH₄ selectivity is lower compared to the non-promoted version. These results suggest that the

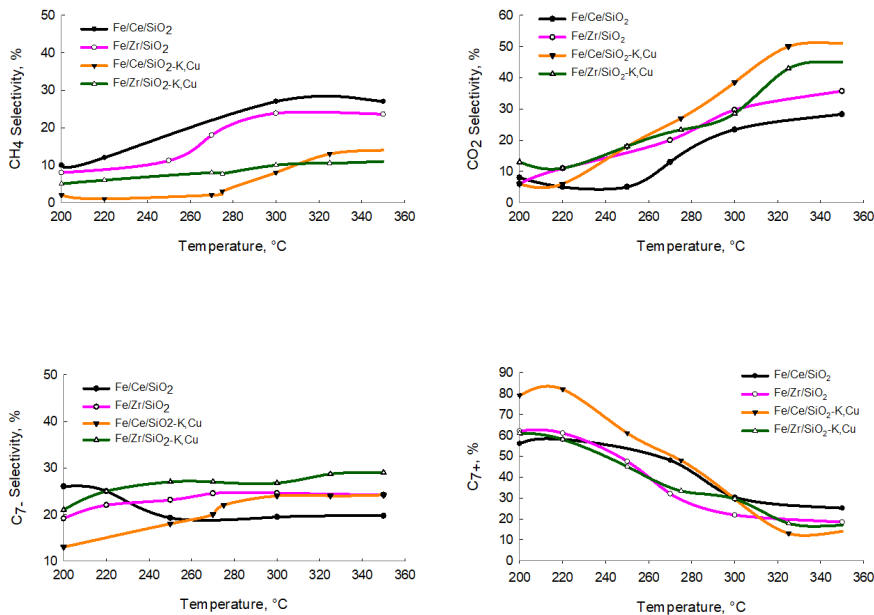


Figure 21: CH₄, CO₂, C₇₋ selectivity and C₇₊ for unpromoted Fe/Ce/SiO₂ and Fe/Zr/SiO₂ vs Fe/Ce/SiO₂-K,Cu and Fe/Zr/SiO₂-K,Cu

promotion of the Fe/Ce/SiO₂-K,Cu and Fe/Zr/SiO₂-K,Cu decreases methane selectivity compared to their non-promoted counterparts.

Overall selectivity towards CO₂ was higher compared to the non-promoted
 455 version. For the Fe/Ce/SiO₂-K,Cu, CO₂ was 6% from 200 °C to 220 °C, and averaged 22% between 250 °C to 275 °C, and 44% from 300 °C to 325 °C. The promoted iron zirconium silicate also had a similar trend; the average CO₂ selectivity was 12% from 200 °C to 220 °C, 18% between 250 °C to 275 °C and 36% from 300 °C to 325 °C. Since the CH₄ selectivity was lower but CO₂ selectivity was higher in comparison to the non promoted catalyst, this indicates
 460 that the selectivity shifted from methane to carbon dioxide. K, is known to produce CO₂ when the loading is above a certain threshold but varies from catalyst to catalyst. The K loading improves both FTS and Water Gas Shift

(WGS) activity but increasing the loading favors WGS instead and produces
465 CO₂ [15, 63, 13, 64]. Therefore, adjusting the K loading could decrease the
CO₂ selectivity. Double promotion with Cu improves the stability and FTS
activity significantly [13, 65, 66, 67].

The light hydrocarbon C₇₋ selectivity for Fe/Ce/SiO₂-K,Cu was quite low
compared to the non promoted catalyst up to 275 °C, after which it increased
470 to 24 % and was invariant while, the non promoted Fe/Ce/SiO₂ decreased to ~
18 %. The C₇₋ selectivity of Fe/Zr/SiO₂-K,Cu was highest at 29 % at 325 °C.
On the other hand, the C₇₊ selectivity reached maximum of 83 % at 220 °C
for Fe/Ce/SiO₂-K,Cu and for Fe/Zr/SiO₂-K,Cu, it was 58 % at 220 °C. The
C₇₊ selectivity decreased as the temperature increased after this point. Adding
475 promoter also increases the CO chemisorption, which explains the shift of C₇₋
to C₇₊ [68].

The analytical data account for the difference in catalytic performance of
metallo-silicate supported iron catalysts. The SEM-EDX demonstrated that
the elements are distributed more homogeneously for Fe/Ce/SiO₂-K,Cu com-
480 pared to the Fe/Zr/SiO₂- K,Cu. In the latter case, metal agglomerates (islands)
formed. A homogeneous distribution facilitates superior catalytic activity for
Fischer Tropsch catalyst because it promotes the contact of the metal oxides
with the reactant gases [69, 70]. Normally, higher BET surface area correlates
with improved performance. However, for the Fe/Ce/SiO₂-K,Cu the BET sur-
485 face area is much lower than the Fe/Zr/SiO₂-K,Cu catalyst. Therefore, the
surface area by itself is insufficient to predict the catalyst performance. BET-
BJH indicated that both structures were mesoporous but the pore size was larger
for the Fe/Ce/SiO₂-K,Cu (15 nm) compared to Fe/Zr/SiO₂-K,Cu (4 nm). The
small pore sizes limits the diffusion of the reactants and the products, which
490 lowers catalytic activity. Larger pore size improves the diffusion of reactants
and limits the re-adsorption of olefins, which produces heavy hydrocarbons be-
cause it induces the production of long carbon chain [53][71] [72] [73]. Also,
XRD indicated that the crystallinity was higher for the cerium silicate sup-
ported catalyst, while it was amorphous for the zirconium silicate supported

495 catalyst. The lack of crystallinity might account for the lower catalytic activity
of Fe/Zr/SiO₂-K,Cu [74].

The stability of metallosilicates and performance of the catalyst differs based
on the active metal. For example, 0.2 g g⁻¹ cobalt was supported on Al, Zr, V
and Ti silicates and tested at 230 °C and 1 MPa. The highest conversion was
500 60 % with Ti silicate support with 83 % selectivity towards C₅₊ [75]. More
recently, another study tested cobalt metallosilicates [34] at 220 °C, 1.83 MPa
for almost 100 h. The CO₂ selectivity was lower (0.3 % for Co/ZrTUD-1 and
4.5 % for Co/CeTUD-1) in comparison to iron metallosilicates. However, the
promoted iron catalysts exhibit a much lower CH₄ selectivity, even at 275 °C
505 for Fe/Zr/SiO₂-K,Cu and 300 °C for Fe/Ce/SiO₂-K,Cu (both ~ 7 % selectiv-
ity). The C₅₊ selectivity is almost the same for both iron and cobalt cerium
silicate catalysts (~ 90 %) at 220 °C. However, the zirconium silicate support
was slightly more stable and the C₅₊ selectivity with cobalt as an active metal
was higher, 88.2 %, compared to iron at 66 %. Furthermore, comparing the Co
510 versus Fe metallosilicates at 220 °C is only valid for the first 6 h since our exper-
iments directed at higher temperature and the catalyst activity changes after
temperature increase [34].

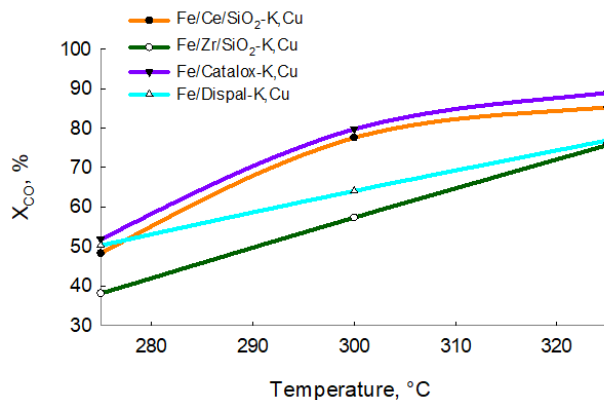


Figure 22: The conversion of CO conversion vs temperature for of promoted Sasol supported
and Metallosilicate supported iron catalysts

We synthesized two additional iron catalysts using commercial Sasol supports, Catalox and Dispall. The CO conversion for the Catalox-supported catalyst reached 88 % at 325 °C while it was 77 % for the Dispall-supported catalyst (Figure 22). While the CO conversion constantly increased with temperature for metallosilicate-supported iron catalysts, the catalysts containing the Sasol supporting materials depended less on temperature.

The average C₇₊ selectivity for the Catalox-supported catalysts was 64 % at 275 °C (Table 6), and further dropped to 22 % at 300 °C. However, as the temperature increased to 325 °C, the C₇₊ selectivity began to rise again reaching 47 %. The Dispall-supported catalyst behaved similarly but with lower C₇₊ selectivity at each temperature (57 %, 17 % and 37 % on average from 275 °C to 325 °C, respectively) (Table 6). For Fe/Catalox-K,Cu, the average CH₄ selectivity was 2 %, 7 % and 8 % from 275 °C to 325 °C in order. The methane selectivity remained similar even as the temperature increased beyond 300 °C. For the Fe/Dispall-K,Cu, the methane selectivity was relatively higher, 4 %, 9 %, 11 % from 275 °C to 325 °C. Although the methane production was similar for both catalysts up to 300 °C, it increased further as the temperature rose to 325 °C for Fe/Dispall-K,Cu. This implies that the catalyst may be susceptible to deactivation if the reaction time was extended at 325 °C.

Table 6: Selectivities of Fe/Catalox-K,Cu and Fe/Dispall-K,Cu

	T (°C)	S_{CO_2}	S_{C7-}	S_{C7+}	S_{CH_4}
Fe/Catalox-K,Cu	275	20	14	64	2
	300	43	28	22	7
	325	35	10	47	8
Fe/Dispall-K,Cu	275	24	15	57	4
	300	46	29	17	9
	325	41	11	37	11

Sasol-supported catalysts showed the highest selectivity for light hydrocarbons (C₂-C₆) at 300 °C (28 % to 29 %), but this temperature also resulted in

high CO₂ selectivity (43 % to 46 %)(Table 6). Increasing the temperature to
535 325 °C decreased the CO₂ selectivity for both catalysts (3 %, 5 % difference, relatively). In summary, raising the temperature from 300 °C to 325 °C shifted the product range towards C₇₊ while methane selectivity remained relatively constant (for Fe/Catalox-K,Cu, while for Fe/Dispall-K,Cu methane selectivity increased) and CO₂ selectivity decreased.

540 The alpha values based on the hydrocarbon distribution were 0.80, 0.76, 0.66 and 0.60 for Fe/Catalox-K,Cu, Fe/Dispall-K,Cu, Fe/Ce/SiO₂-K,Cu and Fe/Zr/SiO₂-K,Cu, respectively (Fig 23). ASF predicts the product distribution based on the calculated alpha values (Fig 24)[76]. The weight percentages of C₅ – C₁₁ are 42 %, 45 %, 40 % and 30 % while C₁₂ – C₁₈ distribution is 22 %,
545 12 %,22 %, 9 % and 2 % for Fe/Catalox-K,Cu, Fe/Dispall-K,Cu, Fe/Ce/SiO₂-K,Cu and Fe/Zr/SiO₂-K,Cu, respectively. The methane percentages for all the catalysts fit with the CH₄ selectivities we found. However, C₂–C₄ selectivities for iron metallosilicates were lower around 15 % compared to the predictions of ASF.

550 The nature of the support has a significant impact on the dispersion, reducibility, acidity and catalytic activity [77]. While there are no previous studies comparing metallosilicate with Al₂O₃, we can still draw some conclusions based on studies comparing SiO₂ and Al₂O₃. For example, one study found that alumina-supported catalysts form FeAl₂O₄, which stabilizes the structure more
555 than silica-supported catalysts [77]. In another study, different supports were tested for iron FT catalysts, and the Al₂O₃ supported catalysts demonstrated higher CO conversion (51 %) than SiO₂ supported catalysts (26 %) after a CO and H₂ pretreatment at 2 MPa, H₂:CO=2 GHSV=16 L h⁻¹ g⁻¹ and T=300 °C. Additionally, the C₅₊ selectivity was 64 % for Fe/Al₂O₃ compared to 60 % for
560 Fe/SiO₂ [10, 78, 79]. As for the reason why metallosilicate supported iron catalysts outperformed plain silica supported iron catalysts, the promotional impact of the metal in the metallosilicates and mesoporous structure that remain intact during the reaction could explain it. The metal in the metallosilicates serves as a promoter that enhances the catalytic activity, while the mesoporous structure

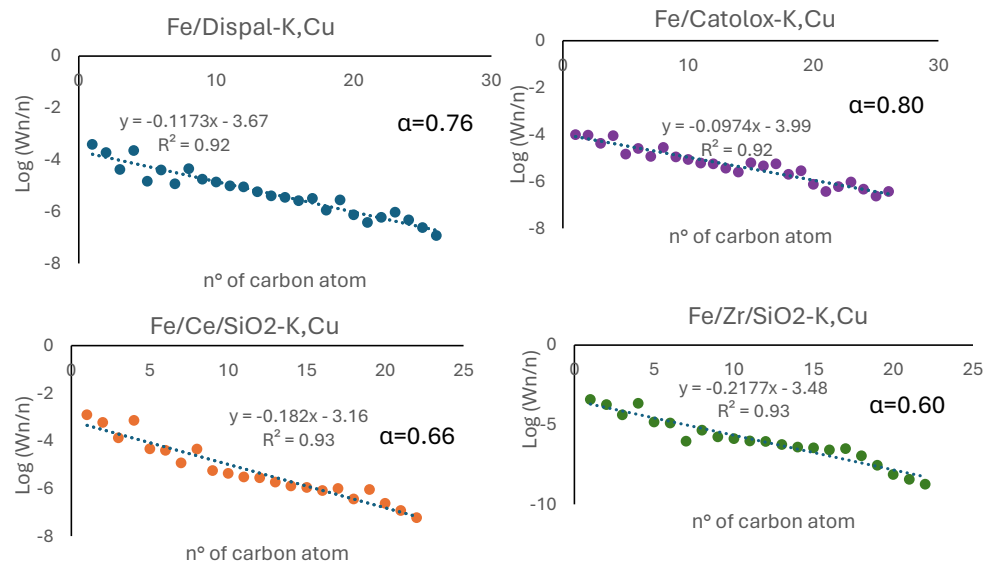


Figure 23: Anderson-Schulz-Flory (ASF) plot of the natural logarithm of the mole fraction for all iron catalysts, Fe/Dispall-K,Cu, Fe/Catalox-K,Cu, Fe/Ce/SiO₂-K,Cu and Fe/Zr/SiO₂-K,Cu

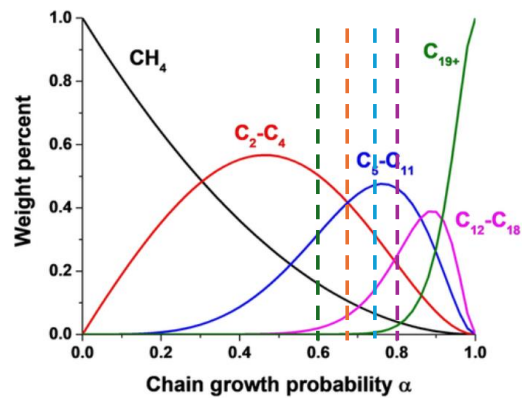


Figure 24: Anderson-Schulz-Flory (ASF) prediction of product distribution for Fischer-Tropsch synthesis, modified based on the color code of each catalyst, turquoise-Fe/Dispall-K,Cu, purple-Fe/Catalox-K,Cu, orange-Fe/Ce/SiO₂-K,Cu and green-Fe/Zr/SiO₂-K,Cu [76]

565 facilitates mass transfer and reactant accessibility to the active sites, resulting
in higher CO conversion and C₅₊ selectivity [80, 81, 17, 82].

The SEM images suggests that the metals are embedded within the alumina support, rendering it more difficult for reactants to reach the active metal sites, which accounts for the lower activity of the alumina-supported catalysts (Figure 18) Although the BET surface of the Catalox supported catalyst was lower
570 than that of the Dispall supported catalyst, Fe/Catalox-K,Cu had an ordered mesoporous structure while the pore structure of Fe/Dispall-K,Cu was ill-defined. This structural difference may have contributed to the higher catalytic activity of the former catalyst. The spherical (donut) morphology of the catalyst particles could improve stability of the Sasol-supported catalyst by offering high
575 surface area to volume ratio, which means that there are more active sites on the catalyst surface. The uniformity of the spherical shape reduces diffusion limitations, pressure drop and increase attrition resistance [83, 54]. Our findings suggest that all the catalysts are characterized by excellent stability during
580 the time of reaction for all the duration of our test (about 90 h) (Supporting document, Figure 6).

4. Conclusion

Iron metallosilicates operate at higher temperatures compared to Co catalysts, which reduces the cooling coil surface area. Typically, Fe catalyst produce
585 more light gases than Co, but the iron metallosilicates, with K and Cu promoters, were capable of producing a hydrocarbon distribution at 300 °C similar to cobalt metallosilicates operating at 220 °C. The K and Cu on the metallosilicates increased conversion 20 % compared to unsupported iron metallosilicates. For example, in our previous study at the same conditions the unsupported iron
590 metallosilicates converted 68 % of the CO for the Fe/Ce/SiO₂ and 52 % for the Fe/Zr/SiO₂ catalysts. It reached 85 % and 75 % at the same conditions 325 °C and 20 bar for these two supports with K and Cu. A further innovation is that rather than a bulk catalyst we applied the NHSG method to synthesize iron

catalyst on commercial Sasol supports Catalox and Dispal. CO conversion over
595 the Catalox exceeded 85 % at 325 °C and 20 bar while the C₇₊ selectivity was
57 %. The catalyst composition was stable with time. On the other hand, the
Dispal supported catalyst converted 78 % of the CO with only 38 % C₇₊ selec-
tivity at the same conditions. Both type of catalysts exhibited similar stability
throughout the reaction process. Metallosilicates have better activity until the
600 temperature 300 °C. To further advance the study of the non-hydrolytic sol-gel
method, optimizing the reaction kinetics through in-depth analysis is essential.
Substituting the iron nitrate with iron chloride is a future avenue of research
to improve catalyst performance. Pt and Mo are other potential promoters to
increase conversion and reduce light gas production. By adjusting the quantity
605 of K and Cu promoters, it may be possible to not only decrease carbon dioxide
production, but also enhance C₇₊ selectivity.

5. Acknowledgment

This research was undertaken, in part, thanks to funding from the Canada
Research Chairs program (950-231476) and Canada Foundation for Innovation
610 (FCI 36788). This work has been partially funded by Piano di Sostegna alla
Ricerca (PSR 2021). Action A of the Dipartimento di Chimica, Università
degli Studi di Milano. The Collegues Prof. Laura Prati and Prof. Alessandro
Minguzzi are warmly thanked for their support contribution to the work with
the PNRR Spoke 9- PE2 project with the Politecnico di Milano.

615 References

- [1] H. Xiong, Y. Zhang, K. Liew, J. Li, Catalytic performance of zirconium-
modified Co/Al₂O₃ for Fisher-Tropsch synthesis, *Journal of Molecular
Catalysis A: Chemical* 231 (2005) 145–151.
- [2] Ø. Borg, S. Eri, E. A. Blekkan, S. Storsæter, H. Wigum, E. Rytter, A. Hol-
620 men, Fisher-Tropsch synthesis over γ -alumina-supported cobalt catalysts:
Effect of support variables, *Journal of Catalysis* 248 (2007) 89–100.

- [3] H. M. T. Galvis, A. C. Koeken, J. H. Bitter, T. Davidian, M. Ruitenbeek, A. I. Dugulan, K. P. de Jong, Effects of sodium and sulfur on catalytic performance of supported iron catalysts for the Fisher-Tropsch synthesis of lower olefins, *Journal of catalysis* 303 (2013) 22–30.
- 625
- [4] F. Lu, X. Chen, Z. Lei, L. Wen, Y. Zhang, Revealing the activity of different iron carbides for Fisher-Tropsch synthesis, *Applied Catalysis B: Environmental* 281 (2021) 119521.
- [5] F. Song, X. Yong, X. Wu, W. Zhang, Q. Ma, T. Zhao, M. Tan, Z. Guo, H. Zhao, G. Yang, et al., FeMn@HZSM-5 capsule catalyst for light olefins direct synthesis via Fisher-Tropsch synthesis: Studies on depressing the co₂ formation, *Applied Catalysis B: Environmental* 300 (2022) 120713.
- 630
- [6] Y. Yang, H.-W. Xiang, Y.-Y. Xu, L. Bai, Y.-W. Li, Effect of potassium promoter on precipitated iron-manganese catalyst for Fischer-Tropsch synthesis, *Applied Catalysis A: General* 266 (2) (2004) 181–194.
- 635
- [7] S. Li, S. Krishnamoorthy, A. Li, G. D. Meitzner, E. Iglesia, Promoted iron-based catalysts for the Fischer-Tropsch synthesis: design, synthesis, site densities, and catalytic properties, *Journal of Catalysis* 206 (2) (2002) 202–217.
- [8] C.-H. Zhang, Y. Yang, B.-T. Teng, T.-Z. Li, H.-Y. Zheng, H.-W. Xiang, Y.-W. Li, Study of an iron-manganese Fischer-Tropsch synthesis catalyst promoted with copper, *Journal of Catalysis* 237 (2) (2006) 405–415.
- 640
- [9] W. Ngantsoue-Hoc, Y. Zhang, R. J. O'Brien, M. Luo, B. H. Davis, Fischer-Tropsch synthesis: activity and selectivity for group I alkali promoted iron-based catalysts, *Applied Catalysis A: General* 236 (1-2) (2002) 77–89.
- 645
- [10] K. Cheng, V. V. Ordonsky, B. Legras, M. Virginie, S. Paul, Y. Wang, A. Y. Khodakov, Sodium-promoted iron catalysts prepared on different supports for high temperature Fisher-Tropsch synthesis, *Applied Catalysis A: General* 502 (2015) 204–214.

- 650 [11] R. J. O'Brien, B. H. Davis, Impact of copper on an alkali promoted iron Fisher-Tropsch catalyst, *Catalysis Letters* 94 (2004) 1–6.
- [12] D. B. Bukur, D. Mukesh, S. A. Patel, Promoter effects on precipitated iron catalysts for Fischer-Tropsch synthesis, *Industrial & Engineering Chemistry Research* 29 (2) (1990) 194–204.
- 655 [13] H. Wan, B. Wu, C. Zhang, H. Xiang, Y. Li, Promotional effects of Cu and K on precipitated iron-based catalysts for Fisher-Tropsch synthesis, *Journal of Molecular Catalysis A: Chemical* 283 (1-2) (2008) 33–42.
- [14] Z. Ni, X. Zhang, J. Bai, Z. Wang, X. Li, Y. Zhang, Potassium promoted core-shell-structured FeK@ SiO₂-GC catalysts used for Fischer-Tropsch synthesis to olefins without further reduction, *New Journal of Chemistry* 660 44 (1) (2020) 87–94.
- [15] S. Li, A. Li, S. Krishnamoorthy, E. Iglesia, Effects of Zn, Cu, and K promoters on the structure and on the reduction, carburization, and catalytic behavior of iron-based Fischer-Tropsch synthesis catalysts, *Catalysis Letters* 665 77 (4) (2001) 197–205.
- [16] H. Chang, Q. Lin, M. Cheng, K. Zhang, B. Feng, J. Chai, Y. Lv, Z. Men, Effects of potassium loading over iron-silica interaction, phase evolution and catalytic behavior of precipitated iron-based catalysts for Fisher-Tropsch synthesis, *Catalysts* 12 (8) (2022) 916.
- 670 [17] T. N. Eran, F. Galli, F. Mazzoni, M. Longhi, A. Grainca, G. Patience, C. Pirola, Metallosilicates as an iron support to catalyze Fisher-Tropsch synthesis, *Catalysis Today* 404 (2022) 132–141.
- [18] E. Tranquillo, F. Bollino, Surface modifications for implants lifetime extension: an overview of sol-gel coatings, *Coatings* 10 (6) (2020) 589.
- 675 [19] D. Navas, S. Fuentes, A. Castro-Alvarez, E. Chavez-Angel, Review on sol-gel synthesis of perovskite and oxide nanomaterials, *Gels* 7 (4) (2021) 275.

- [20] A. Corma, From microporous to mesoporous molecular sieve materials and their use in catalysis, *Chemical Reviews* 97 (6) (1997) 2373–2420.
- [21] A. Taguchi, F. Schüth, Ordered mesoporous materials in catalysis, *Microporous and Mesoporous Materials* 77 (1) (2005) 1–45.
- [22] S. S. Prakash, C. J. Brinker, A. J. Hurd, S. M. Rao, Silica aerogel films prepared at ambient pressure by using surface derivatization to induce reversible drying shrinkage, *Nature* 374 (6521) (1995) 439–443.
- [23] G. Pajonk, Aerogel catalysts, *Applied Catalysis* 72 (2) (1991) 217–266.
- [24] D. P. Debecker, P. H. Mutin, Non-hydrolytic sol–gel routes to heterogeneous catalysts, *Chemical Society Reviews* 41 (9) (2012) 3624–3650.
- [25] V. Smeets, A. Styskalik, D. P. Debecker, Non-hydrolytic sol–gel as a versatile route for the preparation of hybrid heterogeneous catalysts, *Journal of Sol-Gel Science and Technology* 97 (2021) 505–522.
- [26] J. Wentrup, G. R. Pesch, J. Thöming, Dynamic operation of Fischer-Tropsch reactors for power-to-liquid concepts: A review, *Renewable and Sustainable Energy Reviews* 162 (2022) 112454.
- [27] J. Aluha, Y. Hu, N. Abatzoglou, Effect of CO concentration on the α -value of plasma-synthesized CO/C catalyst in Fischer-Tropsch synthesis, *Catalysts* 7 (2) (2017) 69.
- [28] G. S. Pokrovski, J. Schott, F. Farges, J.-L. Hazemann, Iron (iii)-silica interactions in aqueous solution: Insights from x-ray absorption fine structure spectroscopy, *Geochimica et Cosmochimica Acta* 67 (19) (2003) 3559–3573.
- [29] A. S. Kinsela, A. M. Jones, M. W. Bligh, A. N. Pham, R. N. Collins, J. J. Harrison, K. L. Wilsher, T. E. Payne, T. D. Waite, Influence of dissolved silicate on rates of Fe(ii) oxidation, *Environmental Science & Technology* 50 (21) (2016) 11663–11671.

- [30] N. Lohitharn, J. G. Goodwin Jr, E. Lotero, Fe-based Fisher-Tropsch synthesis catalysts containing carbide-forming transition metal promoters, *Journal of Catalysis* 255 (1) (2008) 104–113.
- [31] D. A. Ward, E. I. Ko, Preparing catalytic materials by the sol-gel method, *Industrial & Engineering Chemistry Research* 34 (2) (1995) 421–433.
- [32] C. Milea, C. Bogatu, A. Duta, The influence of parameters in silica sol-gel process, *Bulletin of The Transilvania University of Brasov* 4 (2011) 53.
- [33] S. Vives, C. Meunier, Influence of the synthesis route on sol-gel $\text{SiO}_2\text{-TiO}_2$ (1: 1) xerogels and powders, *Ceramics International* 34 (1) (2008) 37–44.
- [34] G. Kamath, S. Badoga, A. K. Dalai, Synthesis and application of metallosilicate supports for cobalt-based Fisher-Tropsch synthesis catalyst, *Energy & Fuels* 33 (1) (2018) 551–560.
- [35] K. V. Kumar, S. Gadipelli, B. Wood, K. A. Ramisetty, A. A. Stewart, C. A. Howard, D. J. Brett, F. Rodriguez-Reinoso, Characterization of the adsorption site energies and heterogeneous surfaces of porous materials, *Journal of Materials Chemistry A* 7 (17) (2019) 10104–10137.
- [36] R. Bardestani, G. S. Patience, S. Kaliaguine, Experimental methods in chemical engineering: specific surface area and pore size distribution measurements—BET, BJH, and DFT, *The Canadian Journal of Chemical Engineering* 97 (11) (2019) 2781–2791.
- [37] F. J. Sotomayor, K. A. Cychosz, M. Thommes, et al., Characterization of micro/mesoporous materials by physisorption: concepts and case studies, *Accounts of Materials and Surface Research* 3 (2) (2018) 34–50.
- [38] K. S. Sing, R. T. Williams, Physisorption hysteresis loops and the characterization of nanoporous materials, *Adsorption Science & Technology* 22 (10) (2004) 773–782.

- [39] S. Fu, Q. Fang, A. Li, Z. Li, J. Han, X. Dang, W. Han, Accurate characterization of full pore size distribution of tight sandstones by low-temperature nitrogen gas adsorption and high-pressure mercury intrusion combination method, *Energy Science & Engineering* 9 (1) (2021) 80–100.
- [40] K. Karásková, K. Pacultová, T. Bílková, D. Fridrichová, M. Koštejn, P. Peikertová, P. Stelmachowski, P. Kukula, L. Obalová, Effect of zinc on the structure and activity of the cobalt oxide catalysts for NO decomposition, *Catalysts* 13 (2023) 18.
- [41] E. Bertolucci, A. M. R. Galletti, C. Antonetti, M. Marracci, B. Tellini, F. Piccinelli, C. Visone, Chemical and magnetic properties characterization of magnetic nanoparticles, in: 2015 IEEE International Instrumentation and Measurement Technology Conference (I2MTC) Proceedings, IEEE, 2015, pp. 1492–1496.
- [42] K.-S. Loh, Y. H. Lee, A. Musa, A. A. Salmah, I. Zamri, Use of Fe_3O_4 nanoparticles for enhancement of biosensor response to the herbicide 2, 4-dichlorophenoxyacetic acid, *Sensors* 8 (9) (2008) 5775–5791.
- [43] M. Zainuri, Hematite from natural iron stones as microwave absorbing material on x-band frequency ranges, in: IOP conference series: materials science and engineering, Vol. 196, IOP Publishing, 2017, p. 012008.
- [44] V. Kumar, S. Chahal, D. Singh, A. Kumar, P. Kumar, K. Asokan, Annealing effect on the structural and dielectric properties of hematite nanoparticles, in: AIP Conference Proceedings, Vol. 1953, AIP Publishing LLC, 2018, p. 30245.
- [45] G. B. Singh, C. Sonat, E. Yang, C. Unluer, Performance of MgO and MgO– SiO_2 systems containing seeds under different curing conditions, *Cement and Concrete Composites* 108 (2020) 103543.
- [46] G. Jayakumar, A. A. Irudayaraj, A. D. Raj, Particle size effect on the prop-

- erties of cerium oxide (CeO_2) nanoparticles synthesized by hydrothermal method, *Mechanics, Materials Science & Engineering Journal* 9 (1) (2017).
- [47] C. Ashok, K. V. Rao, C. S. Chakra, Structural analysis of CuO nanomaterials prepared by novel microwave assisted method, *Journal of Atoms and Molecules* 4 (5) (2014) 803–806.
- [48] S. A. Ar Sayed, N. I. Beedri, V. S. Kadam, H. M. Pathan, Rose bengal-sensitized nanocrystalline ceria photoanode for dye-sensitized solar cell application, *Bulletin of Materials Science* 39 (2016) 1381–1387.
- [49] I. Joni, L. Nulhakim, M. Vanitha, C. Panatarani, Characteristics of crystalline silica (SiO_2) particles prepared by simple solution method using sodium silicate (Na_2SiO_3) precursor, in: *Journal of Physics: Conference Series*, Vol. 1080, IOP Publishing, 2018, p. 12006.
- [50] S. Ding, J. Zhao, Q. Yu, Effect of zirconia polymorph on vapor-phase ketonization of propionic acid, *Catalysts* 9 (2019) 768.
- [51] O. Mangla, S. Roy, Monoclinic zirconium oxide nanostructures having tunable band gap synthesized under extremely non-equilibrium plasma conditions, *Multidisciplinary Digital Publishing Institute Proceedings* 3 (2018) 10.
- [52] E. I. Mabaso, E. v. Steen, M. Claeys, Fischer-tropsch synthesis on supported iron crystallites of different size (2006).
- [53] Y. Liu, J.-F. Chen, Y. Zhang, The effect of pore size or iron particle size on the formation of light olefins in Fisher-Tropsch synthesis, *RSC Advances* 5 (37) (2015) 29002–29007.
- [54] J.-X. Liu, P. Wang, W. Xu, E. J. Hensen, Particle size and crystal phase effects in Fisher-Tropsch catalysts, *Engineering* 3 (4) (2017) 467–476.
- [55] L. Zhuang, W. Zhang, Y. Zhao, H. Shen, H. Lin, J. Liang, Preparation and characterization of Fe_3O_4 particles with novel nanosheets morphology and

magnetochromatic property by a modified solvothermal method, Scientific Reports 5 (1) (2015) 9320.

- 785 [56] H. Husin, T. Asnawi, A. Firdaus, H. Husaini, I. Ibrahim, F. Hasfita, Solid catalyst nanoparticles derived from oil-palm empty fruit bunches (OP-EFB) as a renewable catalyst for biodiesel production, in: IOP Conference Series: Materials Science and Engineering, Vol. 358, IOP Publishing, 2018, p. 12008.
- 790 [57] S. Suresh, S. Karthikeyan, K. Jayamoorthy, FTIR and multivariate analysis to study the effect of bulk and nano copper oxide on peanut plant leaves, Journal of Science: Advanced Materials and Devices 1 (3) (2016) 343–350.
- [58] J. Sarkar, N. Chakraborty, A. Chatterjee, A. Bhattacharjee, D. Dasgupta, K. Acharya, Green synthesized copper oxide nanoparticles ameliorate defence and antioxidant enzymes in lens culinaris, Nanomaterials 10 (2) 795 (2020) 312.
- [59] S. A. Ansari, Q. Husain, Immobilization of *kluyveromyces lactis* β galactosidase on concanavalin a layered aluminium oxide nanoparticles—its future aspects in biosensor applications, Journal of Molecular Catalysis B: Enzymatic 70 (3-4) (2011) 119–126. 800
- [60] J. Thanuja, G. Nagaraju, H. R. Naika, Biosynthesis of Cu_4O_3 nanoparticles using razma seeds: Application to antibacterial and cytotoxicity activities, SN Applied Sciences 1 (2019) 1–12.
- [61] J. Moulder, J. Chastain, Handbook of X-ray Photoelectron Spectroscopy: 805 A Reference Book of Standard Spectra for Identification and Interpretation of XPS Data, Physical Electronics Division, Perkin-Elmer Corporation, 1992.
- [62] M. Mohai, Xps multiquant: multimodel XPS quantification software, Surface and Interface Analysis: An International Journal devoted to the devel-

- 810 opment and application of techniques for the analysis of surfaces, interfaces
and thin films 36 (8) (2004) 828–832.
- [63] J. Blanchard, N. Abatzoglou, Nano-iron carbide synthesized by plasma as
catalyst for Fisher-Tropsch synthesis in slurry reactors: The role of iron
loading and Cu promoters, *Catalysis Today* 237 (2014) 150–156.
- 815 [64] H. Xiong, M. Moyo, M. A. Motchelaho, L. L. Jewell, N. J. Coville, Fisher-
Tropsch synthesis over model iron catalysts supported on carbon spheres:
The effect of iron precursor, support pretreatment, catalyst preparation
method and promoters, *Applied Catalysis A: General* 388 (1-2) (2010) 168–
178.
- 820 [65] V. R. R. Pendyala, G. Jacobs, M. K. Gnanamani, Y. Hu, A. MacLennan,
B. H. Davis, Selectivity control of Cu promoted iron-based Fisher-Tropsch
catalyst by tuning the oxidation state of Cu to mimic K, *Applied Catalysis
A: General* 495 (2015) 45–53.
- [66] M. Martinelli, C. G. Visconti, L. Lietti, P. Forzatti, C. Bassano, P. Deiana,
825 CO₂ reactivity on Fe–Zn–Cu–K Fisher-Tropsch synthesis catalysts with
different K-loadings, *Catalysis Today* 228 (2014) 77–88.
- [67] Ş. Özkara-Aydınoğlu, Ö. Ataç, Ö. F. Gül, Ş. Kınayyigit, S. Şal, M. Baranak,
İ. Boz, α -olefin selectivity of Fe–Cu–K catalysts in Fisher-Tropsch syn-
thesis: Effects of catalyst composition and process conditions, *Chemical
Engineering Journal* 181 (2012) 581–589.
- 830 [68] W. D. Shafer, M. K. Gnanamani, U. M. Graham, J. Yang, C. M. Masuku,
G. Jacobs, B. H. Davis, Fisher-Tropsch: product selectivity—the fingerprint
of synthetic fuels, *Catalysts* 9 (3) (2019) 259.
- [69] G. Yu, B. Sun, Y. Pei, S. Xie, S. Yan, M. Qiao, K. Fan, X. Zhang, B. Zong,
835 Fe_xO_yC spheres as an excellent catalyst for Fischer-Tropsch synthesis,
Journal of the American Chemical Society 132 (3) (2010) 935–937.

- [70] A. S. Ismail, M. Casavola, B. Liu, A. Gloter, T. W. van Deelen, M. Ver-
shuijs, J. D. Meeldijk, O. Stephan, K. P. de Jong, F. M. de Groot, Atomic-
scale investigation of the structural and electronic properties of cobalt–iron
840 bimetallic Fisher-Tropsch catalysts, *ACS Catalysis* 9 (2019) 7998–8011.
- [71] B. Xu, Y. Fan, Y. Zhang, N. Tsubaki, Pore diffusion simulation model
of bimodal catalyst for Fisher-Tropsch synthesis, *AIChE Journal* 51 (7)
(2005) 2068–2076.
- [72] L. Fan, K. Yokota, K. Fujimoto, Supercritical phase Fischer-Tropsch syn-
thesis: Catalyst pore-size effect, *AIChE Journal* 38 (10) (1992) 1639–1648.
845
- [73] N. Tsubaki, Y. Zhang, S. Sun, H. Mori, Y. Yoneyama, X. Li, K. Fujimoto, A
new method of bimodal support preparation and its application in Fisher-
Tropsch synthesis, *Catalysis Communications* 2 (10) (2001) 311–315.
- [74] J.-Y. Cheon, S.-H. Kang, J. W. Bae, S.-J. Park, K.-W. Jun, G. Murali Dhar,
850 K.-Y. Lee, Effect of active component contents to catalytic performance on
fe-cu-k/zsm5 Fisher-Tropsch catalyst, *Catalysis Letters* 134 (2010) 233–
241.
- [75] K. Okabe, M. Wei, H. Arakawa, Fischer- tropsch synthesis over cobalt
catalysts supported on mesoporous metallo-silicates, *Energy & Fuels* 17 (4)
855 (2003) 822–828.
- [76] Z. Tian, C. Wang, Z. Si, Y. Wang, L. Chen, Q. Liu, Q. Zhang, Y. Xu,
L. Ma, Product distributions of fischer-tropsch synthesis over core-shell
catalysts: The effects of diverse shell thickness, *ChemistrySelect* 3 (44)
(2018) 12415–12423.
- 860 [77] S. Mosallanejad, B. Z. Dlugogorski, E. M. Kennedy, M. Stockenhuber, On
the chemistry of iron oxide supported on γ -alumina and silica catalysts,
ACS Omega 3 (5) (2018) 5362–5374.

- [78] S. C. Kang, K.-W. Jun, Y.-J. Lee, Effects of the CO/CO₂ ratio in synthesis gas on the catalytic behavior in Fischer–Tropsch synthesis using K/Fe –
865 Cu–Al catalysts, *Energy & fuels* 27 (11) (2013) 6377–6387.
- [79] A. Y. Khodakov, W. Chu, P. Fongarland, Advances in the development of novel cobalt Fischer-Tropsch catalysts for synthesis of long-chain hydrocarbons and clean fuels, *Chemical Reviews* 107 (5) (2007) 1692–1744.
- [80] D. V. Peron, A. J. Barrios, A. Taschin, I. Dugulan, C. Marini, G. Gorni,
870 S. Moldovan, S. Koneti, R. Wojcieszak, J. W. Thybaut, et al., Active phases for high temperature Fisher-Tropsch synthesis in the silica supported iron catalysts promoted with antimony and tin, *Applied Catalysis B: Environmental* 292 (2021) 120141.
- [81] F. Farias, R. Rabelo Neto, M. Baldanza, M. Schmal, F. Fernandes, Effect
875 of K promoter on the structure and catalytic behavior of supported iron-based catalysts in Fisher-Tropsch synthesis, *Brazilian Journal of Chemical Engineering* 28 (2011) 495–504.
- [82] A. Wielers, A. Kock, C. Hop, J. Geus, A. van Der Kraan, The reduction behavior of silica-supported and alumina-supported iron catalysts: A
880 Mössbauer and infrared spectroscopic study, *Journal of Catalysis* 117 (1) (1989) 1–18.
- [83] M. Mandic, B. Todic, L. Zivanic, N. Nikacevic, D. B. Bukur, Effects of catalyst activity, particle size and shape, and process conditions on catalyst effectiveness and methane selectivity for Fisher-Tropsch reaction: a modeling study, *Industrial & Engineering Chemistry Research* 56 (10) (2017)
885 2733–2745.